Numerical Simulation of Supercooled Droplets Deformation, Impingement and Freezing for In-Flight Icing

3

Chun-ling Zhu, Ning Zhao, Cheng-xiang Zhu, Lin-lin Tian, and Yi-bin Wang

Contents

Abstract

Water droplet deformation, impingement, and freezing are major processes in the study of in-flight icing. There are complex multi-physics phenomena involving interactions between gas, liquid, and solid. In this chapter, droplet deformation is first numerically investigated. Following this, its effects on airflow velocity, droplet diameter, and ambient temperature are systematically examined through coupling with the level-set method. Based on these studies, new droplet drag analytical models are proposed.

C.-l. Zhu (✉) · N. Zhao · C.-x. Zhu · L.-l. Tian · Y.-b. Wang
Nanjing University of Aeronautics and Astronautics, Nanjing, China
e-mail: clzhu@nuaa.edu.cn; zhaoam@nuaa.edu.cn; cxzhu@nuaa.edu.cn; lins_tian@nuaa.edu.cn; yibin.wang@nuaa.edu.cn

W. G. Habashi (ed.), *Handbook of Numerical Simulation of In-Flight Icing*,
https://doi.org/10.1007/978-3-031-33845-8_44

Besides, for investigating the droplet impingement effect, especially the impingement on surfaces with different hydrophobicity, two numerical techniques (such as level-set and multi-phase Lattice Boltzmann) are employed and developed. The level-set method is used to simulate droplet impact on flat superhydrophobic surfaces; accordingly, a water droplet impingement model governed by Weber and Reynolds numbers is then proposed to predict the outcomes of droplet impingement. In addition, a three-dimensional pseudo-potential Lattice Boltzmann method is developed to investigate the droplet impingement on superhydrophobic surfaces with protrusions, with particular emphasis on the mechanism of contact time reduction.

Finally, the droplet freezing phenomenon is numerically studied through the proposed method, in which the multiphase Lattice Boltzmann and the enthalpy porosity method are adopted to track the gas-liquid and solid-liquid interfaces, respectively. The evolution process of the interface during droplet freezing is visually illustrated, and the effect of droplet size, supercooling degree, and surface hydrophobicity on this process are systematically investigated and analyzed.

Keywords

Droplet · Deformation · Breakup · Weber number · Acceleration · Droplet impact · Superhydrophobic surface · Level-set · Lattice Boltzmann method · Contact time

Introduction

The supercooled water droplet has been reported to be the main cause of aircraft icing (Cao and Xin 2020). Aircraft icing usually occurs when aircraft encounters clouds with supercooled water droplets in flight. The unfrozen supercooled droplets impact the surface of aircraft, and ice accretion occurs through mass and heat exchange phenomena. A better understanding of the droplet deformation and movement mechanisms can significantly improve the efficiency of aircraft icing protection systems.

When a droplet is initially quiescent in a gas flow, it is accelerated by the surrounding gas and deforms. Without considering the effect of gravity, the deformation of the droplet is dominated by the inertial, viscous, and surface tension forces. The well-known non-dimensional Reynolds, Weber and Ohnesorge numbers are defined to characterize the effects of the above forces:

$$Re = \frac{\rho_l U_g D_0}{\mu_l}, We = \frac{\rho_g U_g^2 D_0}{\sigma}, Oh = \frac{\mu_l}{\sqrt{\rho_l \sigma D_0}}$$

where ρ, μ and σ are the density, viscosity, and surface tension coefficient, while the subscripts l and g stand for the liquid and gas phases, respectively. The parameter D_0 is the droplet's initial diameter and U_g is the incoming airflow speed. Previous

Table 1 Different breakup regimes in terms of Weber number

	Vibrational or no breakup mode	Bag breakup mode	Bag-stamen or multi-breakup mode
Krzeczkowski (Krzeczkowski 1980)	$We < 10$	$10 < We < 18$	$18 < We < 30$
Pilch and Erdman (Pilch and Erdman 1987)	$We < 12$	$12 < We < 50$	$50 < We < 100$
Hsiang and Faeth (Hsiang and Faeth 1995)	$We < 11$	$11 < We < 35$	$35 < We < 80$
Chou and Faeth (Chou and Faeth 1998)		$13 < We < 20$	
Dai and Faeth (Dai and Faeth 2001)		$13 < We < 18$	
Zhao et al. (Zhao et al. 2010)	$We < 12$	$12 < We < 16$	$16 < We < 28$
Guildenbecher et al. (Sojka and Guildenbecher 2011)	$We < 9$	$9 < We < 15$	$15 < We < 31$
Jain et al. (Jain et al. 2015)	$We < 12$	$12 < We < 24$	$24 < We < 45$
Li et al. (Li et al. 2022)	$We < 10$	$10 < We < 15$	

research shows that the deformation regimes are usually determined by the Weber number and can be categorized into mainly six modes: vibration, bag breakup, bag-stamen breakup, sheet stripping, and catastrophic breakup. Table 1 presents the ranges of Weber numbers for the three deformation regimes from several authors. It is shown that the droplet deformation transfers from the no breakup regime to the breakup regime as *We* is increased, while the value of the critical *We* varies from different sources.

Over the past decades, numerous experimental and numerical investigations have been conducted on droplet deformation. As early as the 1980s, Krzeczkowski (1980) experimentally studied droplet deformation and breakup in a continuous airflow, with six different liquids. The droplet diameter varied from 2 mm to 5 mm, with the tested Weber number in the range of 13.5~162. It was shown that the droplet deformation and disintegration were dependent on *We*, and the deformation regime map was proposed. Hsiang et al. (Hsiang and Faeth 1995) conducted an experimental study on the effects of density ratios on droplet deformation and breakup with various liquid droplets. Zhao et al. (2010) experimentally studied the deformation of water and ethanol droplets with high-speed digital photography. The dimensionless parameter Rayleigh-Taylor wave number, N_{RT}, was proposed as the criterion for different breakup regimes. Kulkarni et al. (Kulkarni and Sojka 2014) experimentally studied the breakup regimes of water, ethanol, and glycerin droplets with a high-speed digital camera. An empirical model for the dimension growth rate of the deformed droplet was given. Obenauf et al. (Obenauf and Sojka 2021) studied the

deformation of a liquid droplet in continuous uniform air flow, both theoretically and experimentally. A theoretical breakup criterion dependent on the Weber number was developed, and models for droplet velocity and breakup time were proposed. Li et al. (2020) experimentally investigated the droplet deformation and breakup in an opening wind tunnel. A fixed airfoil model was installed inside the wind tunnel to observe the droplet deformation near the airfoil's leading edge. Xu et al. (2020) experimentally investigated the shear effect on droplet behavior in airflows, and a new breakup mode named butterfly breakup was identified.

As an alternative to experimental studies, computational methods are efficient for studying droplet deformation. Regarding the multiphase flows, the treatment of the liquid-gas interface is critical. Nowadays, numerous numerical methods for the interface between phases have been developed. The most used methods are the Volume of Fluid (VOF), Level Set (LS), Coupled Level Set and VOF (CLSVOF), phase field and front tracking. Based on the finite difference/front tracking technique, Han et al. (Han and Tryggvason 1999) numerically studied the breakup of liquid droplets within an axisymmetric system. Quan et al. (Quan and Schmidt 2006) numerically investigated the drag force of droplets when the droplet was accelerated by the gas flow. A density ratio of 50 was simulated, and the moving mesh interface tracking scheme was applied. The results suggested that compared to the solid sphere, the total drag coefficients of the deformed droplet were greater due to the larger recirculation region behind the droplet. Jing et al. (Jing and Xu 2010) numerically studied the breakup of accelerated droplets in continuous gas flow. The axisymmetric governing equations were simulated, and the level-set method was applied for interface capturing. Jalaal et al. (Jalaal and Mehravaran 2014) numerically and theoretically studied the mechanisms of droplet deformation with the VOF method. Kelvin-Helmholtz (KH) and Rayleigh-Taylor (RT) theories were applied to model the instability over the droplet interface by focusing on the initial deformation stage caused by hydrodynamic instability.

In this aspect, the deformation of a water droplet in continuous airflow will be numerically investigated in section "Droplet Deformation." The level-set method is applied for liquid–gas interface capturing. The projection method is applied to solve the incompressible 3D Navier–Stokes equations. The initial droplet diameter and incoming velocity of the continuous airflow vary from 20 μm to 100 μm and 10 to 100 m/s, respectively. A wide range of corresponding Reynolds numbers (221.96–11,098) and Weber numbers (0.033–16.45) are examined. The initially tested parameters are the typical environmental conditions under which aircraft icing occurs. The vibration, transition, bag breakup, and bag-stamen breakup modes of droplet deformation are observed and quantitatively analyzed. The governing equations and adopted numerical models are introduced in section "Governing Equations and Numerical Methods." The validation of the numerical model is presented in section "Validation of the Numerical Model" via a comparison with multiple classical multiphase flow problems, and also our experimental results. Simulation results and discussions are given in section "Microscale Water Droplets Deformation." and the conclusions of this study are described in section "Conclusions."

Additionally, droplet impingement is also a widespread phenomenon in many technical and industrial applications. Examples include spray cooling, internal combustion engines, inkjet printing, spray coating, and painting. In an icing environment, the super-cooled droplets are contained in the clouds. When an aircraft passes through the clouds, the super-cooled droplet impact on the aircraft leads to aircraft icing, which greatly threatens aviation safety. Therefore, the droplet impact dynamic is also investigated in the present chapter. During the impingement process, various phenomena such as spreading, receding, rebound, breakup, and splashing can be observed. The impact outcome is affected by numerous factors such as impact velocity, droplet diameter, droplet viscosity, surface tension, geometric features of the surfaces, and so on. Considering its great significance, droplet impact dynamics have attracted more and more attention.

Similar to the above-mentioned droplet deformation process, the main factors governing the droplet impact dynamics can be characterized by the non-dimensional Reynolds, Weber, and Ohnesorge numbers, which has been shown in Eq. (1). One of the most essential topics of droplet impact is determining the threshold distinguishing the droplet spread/splash regions. Many researchers have established various droplet impact models governed by non-dimensional numbers. Mundo et al. (1995) experimentally investigated the single water and ethanol droplet impact on a dry solid aluminum surface. Based on the measurements to characterize the droplet transition from spreading to splashing, a droplet impingement model was derived, which was given as $K = OhRe^{1.25}$ (where the parameter K is the threshold value). Taking the relative wall surface roughness into consideration, Bai et al. (2002) developed a droplet impingement model for predicting the outcomes of gasoline spray droplets' impact on a solid wall for both dry and wetted surfaces. This model was assessed by simulating experiments on oblique spray impingement in a wind tunnel and showed good accuracy. The topology change of droplets during the impingement process is also a popular research topic, for instance, droplet fingering. For the lower Weber number regime ($We < 160$) in which no splashing or fragmentation occurs, a theoretical model for predicting the number of fingers, K_{cr}, was developed by Huang et al. (2018). This model indicated that no droplet fingers occurred when $We < 60$, and the value of K_{cr} increased along with the droplet size and impact velocity, which was consistent with the experimental results. Especially, due to the significant effects of contact time on droplet hydrodynamics and thermodynamics in many industrial applications, more attention has been given to the reduction of contact time. On a flat solid surface, a theoretical limit of contact time for droplet impacting was proposed with the value of $2.2\tau_0$ $\left(\tau_0 = \sqrt{\frac{\rho_l R_0^3}{\sigma}}\right)$ (Bird et al. 2013). However, several experimental studies reported that asymmetric deformation of droplet impact on a superhydrophobic surface decorated with protrusions could effectively reduce the contact time below the theoretical limit ($2.2\tau_0$) (Gauthier et al. 2015). Bird et al. (2013) conducted a pioneering work in which they investigated the effects of a macroscopic ridge on the contact time for the first time and demonstrated that the contact time could be reduced by 37% compared with droplet impact on flat superhydrophobic surfaces. Gauthier et al. (2015) developed the study of Bird et al.

(2013), and based on their experimental results, they declared the contact time on the superhydrophobic surface with a cylindrical wire can be estimated as $\frac{\tau_{\text{flat}}}{\sqrt{n}}$, where τ_{flat} is the contact time on flat surfaces and n is the number of lobes.

In fact, due to the microscale of the impacting droplets and visualization challenges, it is usually difficult to obtain detailed flow fields and achieve the desired conditions in experiments. As a powerful and efficient method, numerical simulation has become an essential part of the research on droplet impact. Lee and Son (2011) numerically investigated the micro-scaled droplet dynamics on hydrophilic and hydrophobic surfaces, while the liquid-gas interface was captured by a level-set method. Owing to the low impact velocity, they only discussed the droplets' spreading and coalescence behaviors. Zhang et al. (2016) adopted the phase field method to investigate the effects of *We* (1–150) and *Re* (10–1000) on droplet impact on the hydrophobic surface within the axisymmetric coordinate system. In addition to those traditional CFD methods, due to its natural parallel property and ability to deal with complex boundaries, the Lattice Boltzmann method (LBM) has been widely applied in multiphase simulations (Strotos et al. 2016). Based on a Lattice Boltzmann algorithm, Andrew et al. (2017) found that the contact time can be reduced by up to 35% when the radius of the impacting droplet is equal to that of a cylinder. Lin et al. (2019) studied the effects of a single macro-rectangular ridge with two different characteristic sizes on the contact time via a 3D pseudopotential LBM and demonstrated that the contact time can be reduced by more than 40%. Although numerous numerical or experimental studies have been conducted, due to their complexity in nature, the droplet impingement dynamics are still far from completely understood.

To further explore this, the droplet impact on a solid superhydrophobic surface with or without protrusions will be numerically investigated in section "Droplet Impact on Surfaces with Different Hydrophobicity." Due to its outstanding advantages in dealing with complex boundaries, the three-dimensional pseudopotential LBM is adopted to investigate the effects of *We* ($0 < We \leq 67.7$), protrusion size ($10 \leq W \leq 30$), and protrusion shape (triangle, square, and circle) on the droplet dynamics. The level-set method is applied in the investigations of droplet impact on a flat superhydrophobic surface; the effects of ambient temperature, *We* and *Re* will be analyzed in detail. First, the numerical methods, including the level-set and pseudopotential LBM, will be introduced in sections "Governing Equations and Numerical Methods" and "Pseudopotential Lattice Boltzmann Method and Curved Boundary Treatment" respectively. Then droplet impact dynamics on a flat superhydrophobic surface will be discussed, followed by the discussion of droplet dynamics and contact time reduction mechanism on superhydrophobic surfaces with protrusions. Finally, concluding remarks will be made.

Besides, droplet freezing on the wing surface is another fundamental problem in aircraft icing. A detailed description of the freezing process will provide helpful guidance for anti-icing and de-icing applications. Numerous experimental works have been reported regarding droplet freezing (Jung et al. 2012). Huang et al. (2012) conducted a series of freezing experiments on surfaces with different contact angles.

It was found that the contact angle can significantly influence the droplet's total freezing time, and the freezing on the surface with a larger contact angle starts later. Zhang et al. (2018, 2019) analyzed different-sized supercooled droplet freezing on the surface with different cooling temperatures. They reported that compared to the droplet volume, the plate temperature and contact angle play a more significant role in freezing. Stiti et al. (2020) adopted a new experimental technique to acquire the liquid-ice interface within the freezing droplet and observed that it appeared to have a spherical shape. They also observed that different surfaces could affect the formation of the protrusion tip after the droplet turned into ice.

Furthermore, numerical solutions could provide more comprehensive information on the initiation and development of the ice and reveal the droplet freezing rules (Zhao et al. 2017; Rakotondrandisa et al. 2019; Wang et al. 2020). Sun et al. (2015) conducted the simulations by LBM, which applied the velocity and temperature distribution functions. The results suggested that freezing occurs earlier at lower plate temperatures, and the phase transition develops at a decreasing rate. Zhang et al. (2020a) developed an axisymmetric LBM for simulations with the density ratio of the droplet to air (DR) being equal to 20 and indicated that the ice and droplet profile form an acute angle which keeps almost constant. For a natural density ratio of about 1000, Blake et al. (2015) studied the supercooled droplet freezing and bouncing. The results showed that the droplet was more likely to be attached under lower plate temperatures. However, the works mentioned above do not involve the effects of droplet supercooling and volume expansion when simulating the droplet freezing from CFD governing equations with natural liquid-gas density ratio, which is a more straightforward way to reveal the development of the phase transition and temperature distribution evolution.

To solve this problem, considering the volume expansion of the droplet during droplet freezing, a numerical method is proposed through the combination of a multiphase Lattice Boltzmann flux solver and the phase field method; based on this, the droplet freezing process on the cold surface is then studied in section "Droplet Freezing." Validations of this proposed numerical model are presented in section "Validation of the Method" by comparing with experimental data. Afterward, three main impact factors (respectively the droplet size, supercooling degree, and surface hydrophobicity) and their impact on the freezing process of droplets are systematically investigated in section "Results and Discussions." The conclusions of this study are summarized in section "Conclusions."

Droplet Deformation

Governing Equations and Numerical Methods

Firstly, the level-set method (Sussman et al. 1994) for multiphase interface capturing is introduced. The level-set function ϕ is defined as the signed distance function based on the location of interface Γ

$$\phi(\mathbf{x},\mathrm{t}) = \begin{cases} |\mathbf{x}-\mathbf{x}_\Gamma|, \mathrm{x} \in \text{air phase} \\ 0, \mathrm{x} \in \Gamma \\ -|\mathbf{x}-\mathbf{x}_\Gamma|, \mathrm{x} \in \text{liquid phase} \end{cases} \tag{1}$$

The smoothed Heaviside function $H(\phi)$ is applied to smooth the discontinuous physical properties near the interface within a certain thickness 2ε

$$H(\phi) = \begin{cases} 1, \phi > \varepsilon \\ \frac{1}{2}\left[1 + \frac{\phi}{\varepsilon} + \frac{1}{\pi}\left(\frac{\pi\phi}{\varepsilon}\right)\right], |\phi| \le \varepsilon \\ 0, \phi < -\varepsilon \end{cases} \tag{2}$$

Then the density and viscosity fields are determined according to the value of the level-set function:

$$\begin{aligned} \rho(\phi) &= \rho_l + \left(\rho_g - \rho_l\right)\mathrm{H}(\phi) \\ \mu(\phi) &= \mu_l + \left(\mu_g - \mu_l\right)\mathrm{H}(\phi) \end{aligned} \tag{3}$$

where the subscripts l and g denote the liquid and air phases, respectively. In the present study, the interface thickness is set as $\varepsilon = \Delta x$.

The conservative form of the level-set advection equation is solved for the liquid-gas interface evolving:

$$\frac{\partial \phi}{\partial \mathrm{t}} + \nabla \cdot (\mathbf{u}\phi) = 0 \tag{4}$$

The WENO5 scheme for conservative advection equation (Solomenko et al. 2017) is applied for spatial discretization, and a third-order TVD Runge-Kutta scheme is used for temporal discretization. In addition, the Hamilton-Jacobi equation is solved for ϕ^{n+1} to maintain the level-set function as a signed distance function.

$$\frac{\partial \phi}{\partial \tau} + \mathrm{Sign}(\phi)(|\nabla\phi| - 1) = 0 \tag{5}$$

where $\mathrm{Sign}(\phi)$ is the sign function and τ is the pseudo marching time. The third-order TVD Runge-Kutta scheme is used for temporal discretization, while the fifth-order WENO scheme(Fedkiw et al. 1999) is applied for the first-order spatial derivatives.

The continuity and momentum equations for incompressible, immiscible multi-phase flow are written as:

$$\nabla \cdot \mathbf{u} = 0 \tag{6}$$

$$\frac{\partial \rho \mathbf{u}}{\partial \mathrm{t}} + \nabla \cdot \rho\mathbf{u}\mathbf{u} = -\nabla \mathrm{p} + \nabla \cdot \left[\mu\left(\nabla\mathbf{u} + \nabla\mathbf{u}^{\mathrm{T}}\right)\right] + \rho\mathbf{g} + \mathbf{f}_\mathrm{s} \tag{7}$$

in which **u** is the velocity vector, p is the pressure, g is the gravitational acceleration, and $\mathbf{f}_s$ is the surface tension force acting on the liquid-gas interface. The continuum surface tension force (CSF) model (Brackbill et al. 1992) is applied to the surface tension force:

$$\mathrm{f_s} = \sigma\kappa\nabla\widetilde{\mathrm{C}} \tag{8}$$

with

$$\kappa = -\nabla\cdot\mathbf{n}, \mathbf{n} = \frac{\nabla\phi}{|\nabla\phi|} \tag{9}$$

where σ is the surface tension coefficient, κ is the interface curvature and **n** is the normal unit vector. The normal vector to the interface is computed with the signed distance function ϕ. The function $\widetilde{\mathrm{C}}$ is a mollified version (Nangia et al. 2019) of the Heaviside function that ensures the surface tension force is applied only near the zero level set within a certain interface thickness.

For the solution methodology for governing equations, the staggered grid system is applied, as shown in Fig. 1. The variables $\rho_{i,j}$, $p_{i,j}$, $\phi_{i,j}$, $\mu_{i,j}$ are located at the cell center, while the velocity components $u_{i+\frac{1}{2},j}$ and $v_{i,j+\frac{1}{2}}$ are located at the cell centers. The well-known projection method is used to solve the momentum equation. Firstly, the pressure gradient term is decoupled from the original momentum eq. (8) and yields:

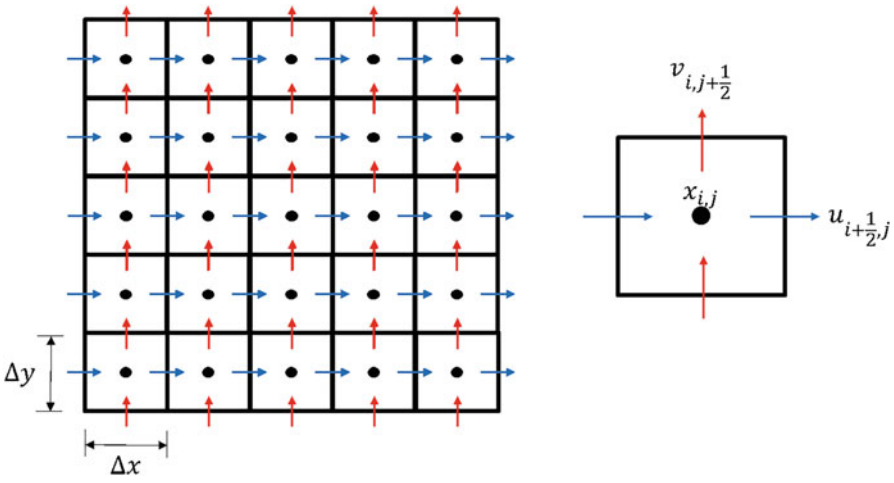

Fig. 1 (**a**) A staggered-grid discretization of the computational domain. (**b**) A schematic of the Cartesian grid cell.

$$\frac{\rho(\mathbf{u}^{*}-\mathbf{u}^{n})}{\Delta t}=R^{n} \tag{10}$$

$$\frac{\rho(\mathbf{u}^{n+1}-\mathbf{u}^{*})}{\Delta t}=-\nabla p^{n+1} \tag{11}$$

Where $R^{n}=-\nabla\cdot\rho\mathbf{u}\mathbf{u}+\nabla\cdot[\mu(\nabla\mathbf{u}+\nabla\mathbf{u}^{T})]+\rho\mathbf{g}+\mathbf{f}_{s}$, and $\mathbf{u}^{*}$ is the intermediate velocity after decoupling. The intermediate velocity is implicitly solved by the Crank-Nicolson scheme. An explicit third-order cubic upwind interpolation (CUI) scheme (Patel and Natarajan 2017) is applied to compute the convective derivative. The CUI scheme of $(\nabla\cdot u\psi)_{i-1/2,j}$ is summarized below as an example where ψ is the advected variable that could be the x-component velocity or the density on the faces. The approximation of the normalized value is given as:

$$\widetilde{\psi}_{f}=\begin{cases}3\widetilde{\psi}_{C}, & 0<\widetilde{\psi}_{C}\le\dfrac{2}{13}\\ \dfrac{5}{6}\widetilde{\psi}_{C}+\dfrac{1}{3}, & \dfrac{2}{13}<\widetilde{\psi}_{C}\le\dfrac{4}{5}\\ 1, & \dfrac{4}{5}<\widetilde{\psi}_{C}\le 1\\ \widetilde{\psi}_{C}, & \text{otherwise}\end{cases} \tag{12}$$

in which the normalized value is defined as:

$$\widetilde{\psi}=\frac{\psi-\psi_{U}}{\psi_{D}-\psi_{U}} \tag{13}$$

where the upwind ψ_{C}, far upwind ψ_{U} and downwind ψ_{D} are labeled depending on the direction of the advection velocity. Finally, the approximation of $(\nabla\cdot u\psi)_{i-1/2,j}$ is computed as below, where the subscript w, e, n, and s stand for the interpolated values on the faces of the shifted control cell.

$$(\nabla\cdot u_{adv}\psi_{lim})_{i-\frac{1}{2},j}=\frac{u_{e}\psi_{e}-u_{w}\psi_{w}}{\Delta x}+\frac{v_{n}\psi_{n}-v_{s}\psi_{s}}{\Delta y} \tag{14}$$

Then, combining Eq. (12) with the continuity equation Eq. (7), we have the pressure Poisson equation:

$$\frac{\nabla\cdot\mathbf{u}^{*}}{\Delta t}=\nabla\cdot\left(\frac{\nabla p^{n+1}}{\rho}\right) \tag{15}$$

The conjugate gradient (CG) method solves the above implicit pressure equation, and then the velocity field is updated via Eq. (12).

In numerical simulations, the high-density ratio between liquid and gas phases often results in significant numerical oscillations at the liquid-gas interface. To avoid this problem, the conservative discretization method proposed by Nangia et al.

(2019) is employed and applied to achieve robust simulations. The additional discretized density update equations on faces of the staggered gird are solved with the third-order accurate strong stability preserving Runge-Kutta (SSP-RK3) time integrator

$$\breve{\rho}^{(1)} = \breve{\rho}^{n} - \Delta t R\left(u_{adv}^{n}, \breve{\rho}_{lim}^{n}\right) \tag{16}$$

$$\breve{\rho}^{(2)} = \frac{3}{4}\breve{\rho}^{n} + \frac{1}{4}\breve{\rho}^{(1)} - \frac{1}{4}\Delta t R\left(u_{adv}^{(1)}, \breve{\rho}_{lim}^{(1)}\right) \tag{17}$$

$$\breve{\rho}^{n+1,k+1} = \frac{1}{3}\breve{\rho}^{n} + \frac{2}{3}\breve{\rho}^{(2)} - \frac{2}{3}\Delta t R\left(u_{adv}^{(2)}, \breve{\rho}_{lim}^{(2)}\right) \tag{18}$$

Here, the subscript "adv" indicates the interpolated advective velocity on the faces of the face-centered control volume, and the subscript "lim" means the limited value, as defined by Eq. (15).

The adaptive time step is determined following the works of Kang et al. (2000). The restriction to the time step is based on convection, viscosity, and surface tension:

$$\Delta t\left(\frac{(C_{cfl} + V_{cfl}) + \sqrt{(C_{cfl} + V_{cfl})^2 + 4(S_{cfl})^2}}{2}\right) \leq \frac{1}{2} \tag{19}$$

where C_{cfl}, V_{cfl} and S_{cfl} are convection, viscosity, and surface tension time step restriction, respectively. The corresponding definitions are given as:

$$C_{cfl} = \frac{|u|_{max}}{\Delta x} + \frac{|v|_{max}}{\Delta y} + \frac{|w|_{max}}{\Delta z} \tag{20}$$

$$V_{cfl} = \max\left\{\frac{\mu_l}{\rho_l}, \frac{\mu_g}{\rho_g}\right\} \cdot \left(\frac{2}{(\Delta x)^2} + \frac{2}{(\Delta y)^2} + \frac{2}{(\Delta z)^2}\right) \tag{21}$$

$$S_{cfl} = \sqrt{\frac{\sigma|\kappa|}{\rho_g \cdot (\min\{\Delta x,\ \Delta y,\ \Delta z\})^2}} \tag{22}$$

Validation of the Numerical Model

Before using this method for simulations of water droplet deformation, several commonly studied multiphase flow problems are investigated to verify the accuracy, consistency, and stability of the present numerical method. The accuracy of present numerical method is also validated via the comparison with corresponding experimental results. Related results and discussions are given below.

Rayleigh-Taylor Instability

The Rayleigh-Taylor instability problem is simulated here to test the numerical model. The Rayleigh-Taylor instability of binary fluids is generated by gravity when the heavy fluid is on top of the light one. The problem is simulated within a rectangular computation domain $[0, d] \times [0, 4d]$. The domain size d is chosen as 1 and the grid resolution is 100×400, while the time step is fixed as Δt=0.001. The dimensionless number Atwood number is defined for the density ratio between two fluids as $At = (\rho_H - \rho_L)/(\rho_H + \rho_L)$, in which H denotes the heavy fluid above the interface and L denotes the light one. In this simulation At number is chosen as 0.5, which corresponds to a density ratio of 3, and a viscosity ratio $\mu_H/\mu_L = 3$. For this gravity-induced problem, the Reynolds number is defined as $Re = \sqrt{dg} \cdot d/\nu$, in which g is the gravity that is set as 1, ν is the kinematic viscosity as $\nu = \mu/\rho$ and Re is fixed as 256. The initial location of the interface is set as $y = 2 + 0.1\cos(2\pi x)$, and the initial velocity of two different fluids is zero. The left and right boundaries are set as symmetric, while the top and bottom boundaries are set as non-slip conditions.

The simulated temporal evolutions of the interface are given in Fig. 2. At the early stages, the heavy fluid above the interface starts to fall due to gravity, and a spike forms on the interface. In the meantime, the rising bubbles of light fluid are formed along the two vertical boundaries. Then, two counter-rotating vortices are generated adjacent to the falling spike of the interface due to the rolling-up of heavy fluid. As the evolution continues, the two counter-rotating vortices are separated from the heavy fluid, and a pair of secondary vortices are formed at the ends of the roll-ups.

The simulated temporal evolutions of the spike and edge of the interface are presented in Fig. 3 and compared with the published results from Patel. et al. (Patel

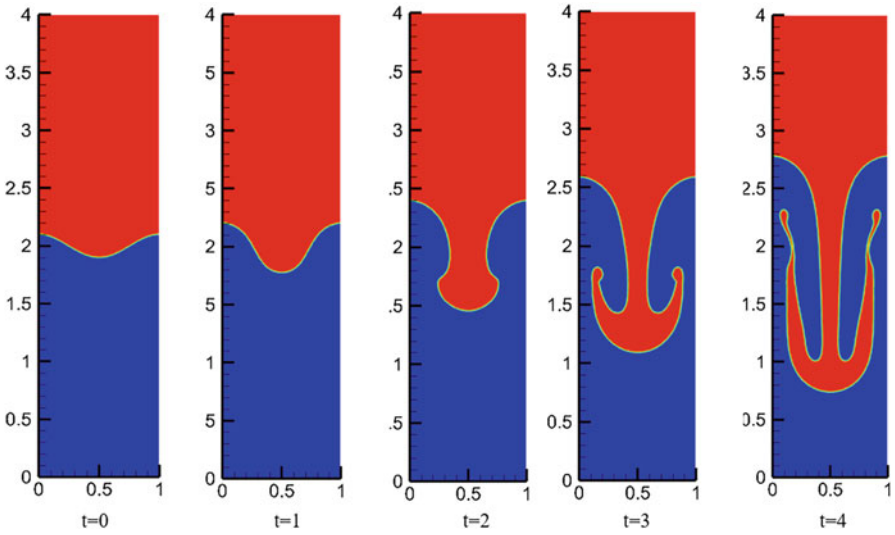

Fig. 2 Fluids interface of Rayleigh-Taylor instability with $Re = 256$

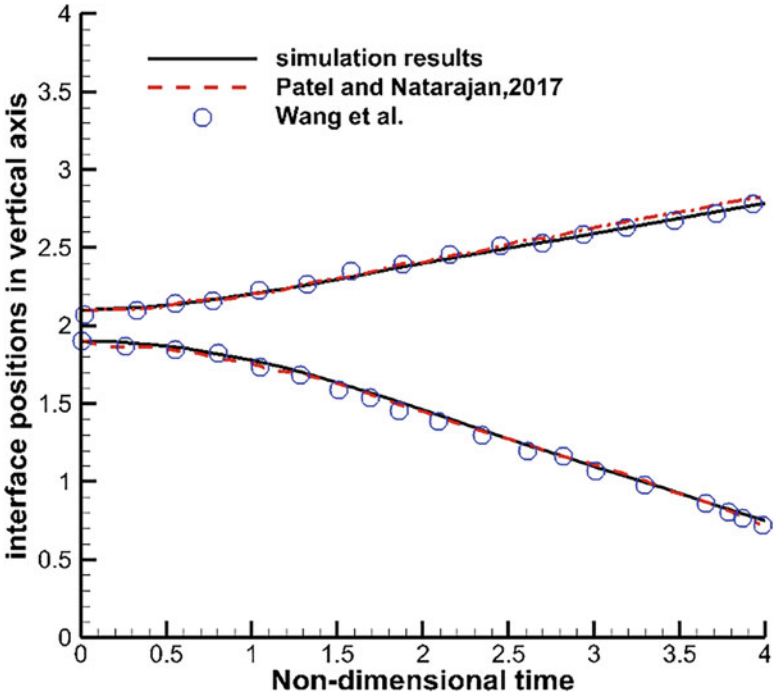

Fig. 3 Temporal evolutions of the spike and edge of the interface

and Natarajan 2017). The comparison shows a good agreement between the present numerical results and the results from the literature.

Droplet Splashing on a Thin Water Film

Droplets impacting a thin layer of liquid are commonly observed in many industrial applications such as inkjet printing and fuel injection. Its numerical simulation is challenging due to the large density and viscosity ratios across the liquid-gas interface, which may generate singularity at the impact point. In this section, the problem of a water droplet splashing on a thin water film is simulated to verify the accuracy of the present model for a high-density ratio. For this simulation, the rectangular domain size is $[0, 8D]\times[0, 2D]$ with grid size 800×200, and the diameter D of the droplet is 1. The initial location of the droplet center is at $[4D, 0.75D]$, and the thickness of the initial liquid film is $0.1D$. The physical properties of water and air are adopted for the liquid and gas phases, respectively. The dimensionless number Webber number $We = \frac{\rho_g U^2 D}{\sigma} = 0.126$, and two values 6.6 and 66 are tested for Reynolds number $Re = \frac{\rho_g UD}{\mu_g}$. The initial downward velocity of droplet $U = 1$ and the gravity are neglected. The time step $\Delta t = \Delta x/50$, and the no-slip boundary conditions are imposed on each boundary of the domain. The simulated temporal evolutions of the interface are given in Fig. 4.

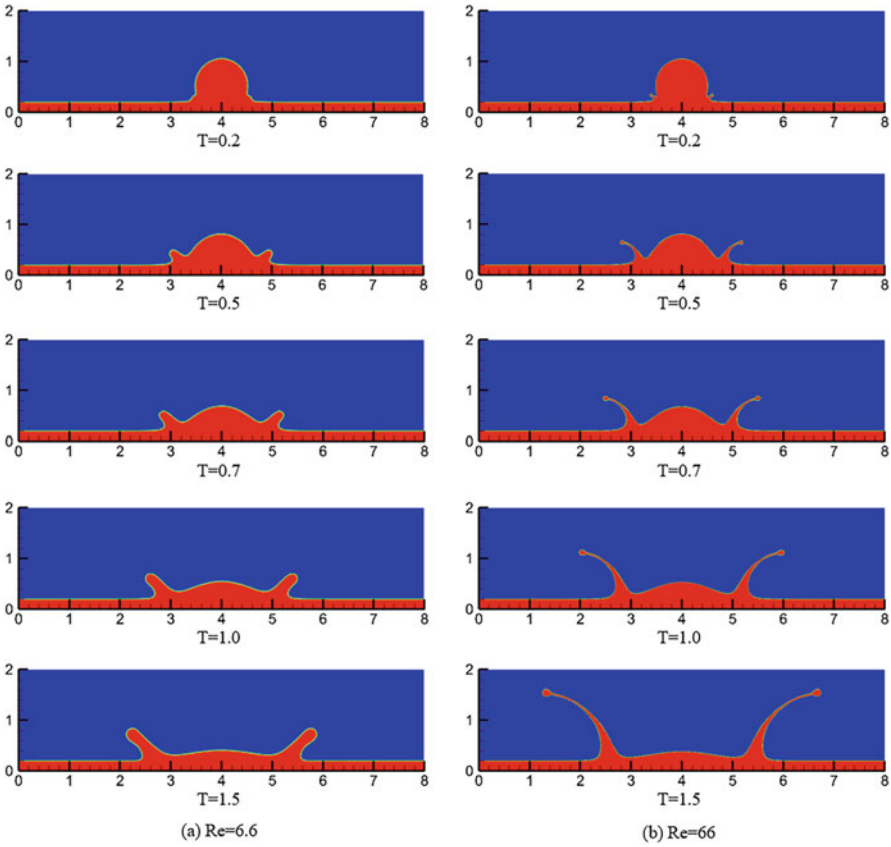

Fig. 4 Evolution of droplet movement and film splashing process (**a**) Re = 6.6; (**b**) Re = 66

Figure 4 shows the interactions among moving droplets and liquid film and the slashing process of liquid film at different simulation times. From Fig. 4a it is seen that for low Reynolds number, the droplet hits the liquid film surface and then merges into the film. During the following temporal evolution, a pair of symmetric waves called "liquid fingers" are formed on the film surface and move outward to the vertical boundaries. Under this circumstance, the liquid fingers are strong enough to withstand the surface tension and viscous force, so no droplet satellites are observed during the evolution. The simulation results of Fig. 4a match well with the numerical works of Patel et al. (Patel and Natarajan, 2017) and Nangia et al. (2019). For higher Reynolds number $Re = 66$ as shown in Fig. 4b, it is seen that the splashing phenomenon happens at a higher Reynolds number and the "crown" is observed. Compared to the case with a lower Reynolds number, the length of the splashed liquid finger is increased while the thickness becomes smaller. At $T = 1.5$, a tiny liquid droplet attached to the end rim of the liquid finger can be observed. The jet base location x_j investigated by Coppola et al. (2011) is graphically displayed in

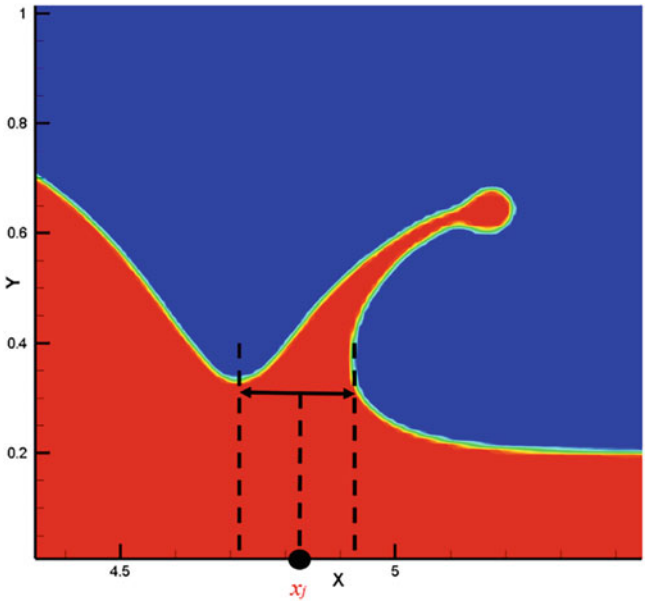

Fig. 5 Jet base location of splashing rim

Fig. 5. The value is computed by averaging the x-position of the two neck points of the splashing rims. The normalized jet base location $(x_j - x_0)/D$ is presented in Fig. 6 versus the normalized time $\sqrt{Ut/D}$, which x_0 is the initial x-position of the droplet center. According to the theoretical studies of Josserand and Zaleski (2003), the normalized jet base location x_j should scale with the square root of the normalized time. The comparison given in Fig. 6 indicates that the present numerical results have a better agreement with both the power law and the numerical results of Nangia et al. (2019).

The Collapse of a Water Column

The water column collapsing problem caused by gravity is investigated here. The simulation for the collapse of a liquid column is challenging due to the interface's free-surface flow and large distortions, especially with a large density ratio. The rectangular domain has a size of $[0, 7a]\times[0, 2a]$, in which a is the length of the initial square water column and $a = 1$. The grid size is 350×100, while time step $\Delta t = \Delta x/100$. The density ratio 815 and viscosity ratio 55 are applied while $\rho_g = 1$ and $\mu_g = 1.78 \times 10^{-5}$. The surface tension coefficient of water is $\sigma = 0.0728$. The gravity value is set as 9.8, and the water column and ambient air are initially stationary. The no-slip boundary conditions are imposed for all boundaries of the simulation domain. The temporal evolution of the collapsing water column is shown in Fig. 7. The dimensionless time is normalized by $t = \mathrm{T}/\sqrt{\mathrm{a}/\mathrm{g}}$. It is shown that the initially unstable water column collapses under the effect of gravity. During the movement, the liquid interface remains smooth and develops stably.

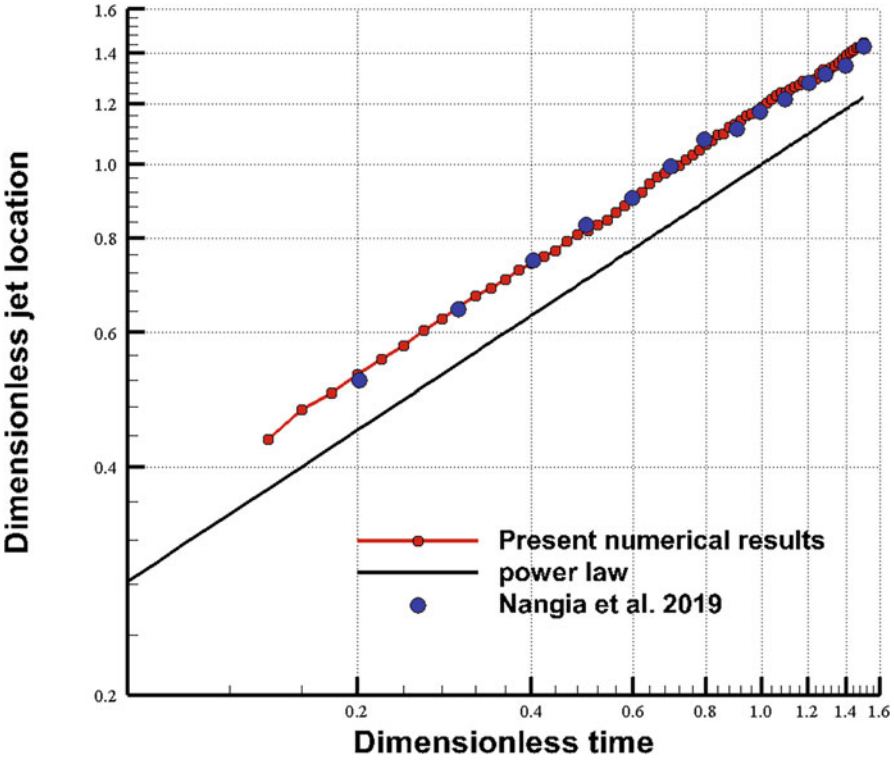

Fig. 6 Dimensionless jet base location versus time for $Re = 66$

The temporal evolutions of the water column height and the front position are shown in Fig. 8. It is shown that after the collapse is triggered, the front position is almost linearly increased during the spreading on the bottom surface. Meanwhile, the changing rate of the column height first increases during the preliminary stage of development; then the rate later decreases when the water film forms above the surface. The experimental results of Martin and Moyce Penney (1952) and the numerical results of Nangia et al. (2019) are also presented in Fig. 8. The comparison gives a good agreement between the present simulation results and the published results in previous literature.

Deformation of Water Droplet in Incoming Airflow

The experimental setup used to study the droplet deformation process is shown in Fig. 9. The open-loop wind tunnel with a horizontal rectangular nozzle is designed to generate a continuous airflow. The outlet cross-section is 300 mm in width and 75 mm in height. The airflow is generated by a centrifugal blower and an inverter motor. A honeycomb mesh is placed in the upstream duct of the contraction and nozzle to produce a uniform airflow. The maximum velocity that can be produced at the nozzle exit is 45 m/s.

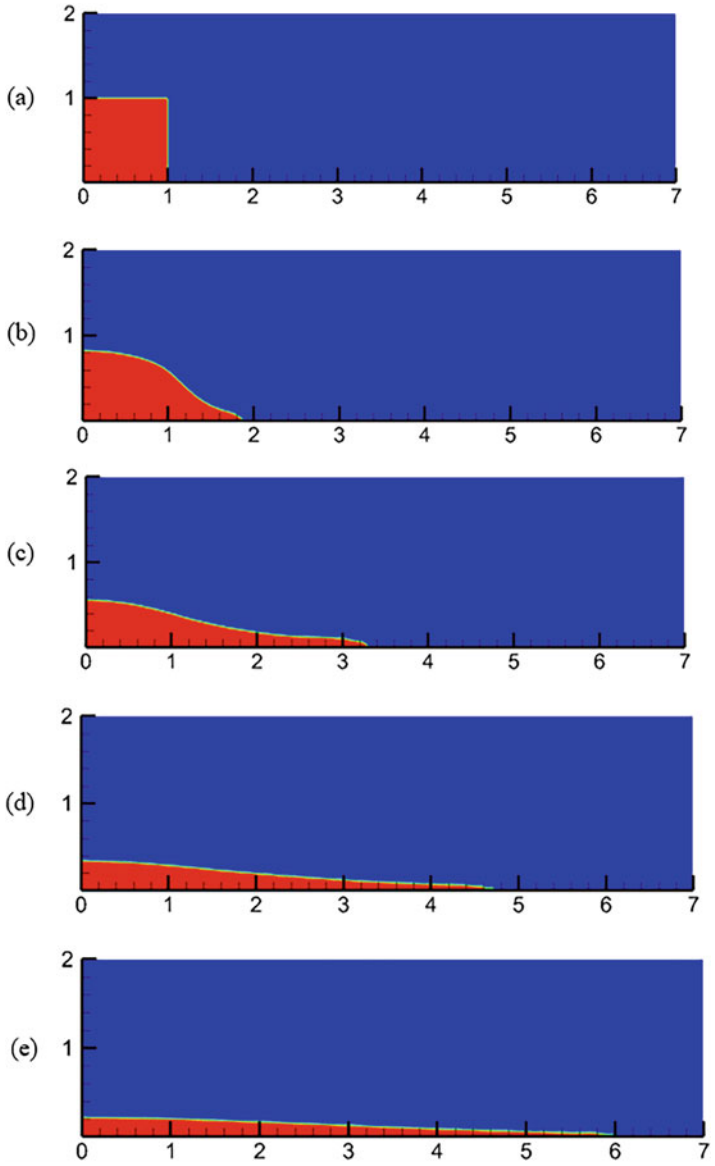

Fig. 7 Evolution of collapsing water column (**a**) $t = 0$; (**b**) $t = 1$; (**c**) $t = 2$; (**d**) $t = 3$; (**e**) $t = 4$

Deionized water is used as the droplet fluid. The fluid is driven by a syringe pump, with a droplet formed at the tip of a dispensing needle (inner diameter of 0.11 mm). The droplet detaches from the needle and falls into the airflow under gravity. The distance between the airflow stream and the nozzle exit is 17 mm. The height of the droplet generator can be adjusted to ensure the droplet passes through

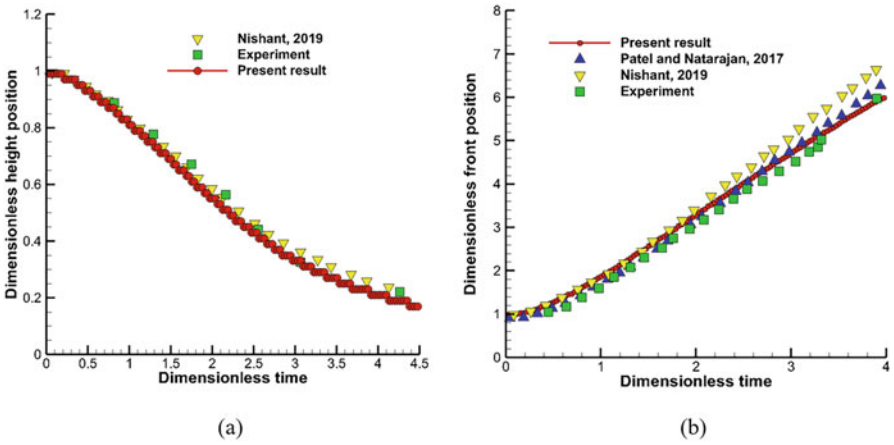

Fig. 8 The position evolution of collapsing water column (**a**) height position, (**b**) front position

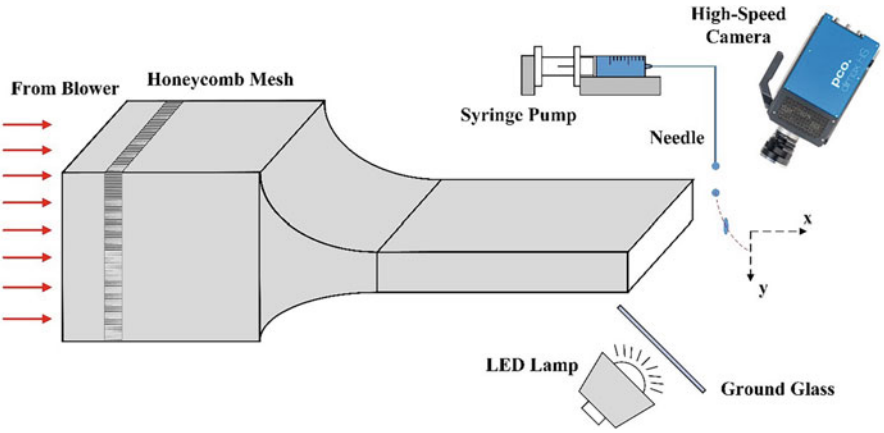

Fig. 9 Schematic diagram of the experimental setup

the boundary layer quickly, so that the effect of the boundary layer is negligible. The diameter of the droplets generated in this study is $D_0 = 2.2 \pm 0.1$ mm and the downward velocity of the droplet is approximately 2.1 m/s. A high-speed camera (PCO. DIMAX) is used to record the deformation process of the droplet. The frame rate of the camera is 4000 fps and the image resolution is 17.06 μm per pixel. The visibility of the droplets is enhanced by a backward-facing LED light source with a ground glass. The experiments are performed at room temperature and atmospheric pressure.

Figure 10 presents the numerical results for the temporal evolution of the droplet configuration, as well as a comparison with the experimental results. The initial diameter of the water droplet and the incoming velocity of the airflow agree with the experimental conditions: $D_0 = 2.22$ mm and $U_g = 13.2$ m/s. The boundary

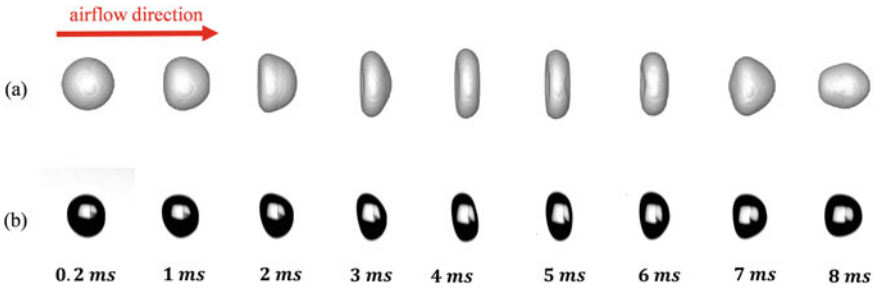

Fig. 10 Comparison of droplet deformation: (**a**) numerical results, (**b**) experimental results ($We = 6.36$)

conditions and numerical domain follow the setup described in section "Microscale Water Droplets Deformation." It is seen from Fig. 10 that at the preliminary stage of acceleration, the windward side of the droplet becomes flat while the whole droplet is elongated in the cross-stream direction. At time $t = 3$ ms, the droplet deforms into a typical "hat shape," with a bulge on the leeward side. The droplet is then further stretched in the cross-stream direction and deforms into an ellipsoid ($t = 4$ ms). As the development continues, the bulge forms again on the leeward side of the droplet ($t = 7$ ms), and then the droplet becomes elongated in the streamwise direction ($t = 8$ ms). The numerical results for the temporal evolution of the droplet configuration are in good agreement with the experimental results.

Microscale Water Droplets Deformation

The microscale water droplets deformation in uniform airflow is numerically investigated in the present section. A schematic illustration for the corresponding 3D simulation domain is provided in Fig. 11. The size of the computational domain is $(L_x, L_y, L_z) = (10D_0, 5D_0, 5D_0)$, and the grid resolution is 40 grids per droplet diameter. The droplet is quiescent at the beginning, and its center is placed at a distance of D_0 from the left boundary. The uniform airflow with constant inlet velocity U_g moves into the simulation domain from the left boundary ($x = 0$), which is set as the inlet boundary condition (marked as the blue plane in Fig. 11). The pressure outlet boundary condition is applied for all other boundaries. Different droplet initial diameters and uniform airflow velocities are tested, and the effects of initial droplet diameter, non-dimensional numbers, and supercooling on droplet deformation and acceleration are studied.

The physical properties such as density, viscosity, and surface tension coefficient corresponding to room temperature $T = 25$ °C and icing temperature $T = -25$ °C are adopted for the liquid and gas phases. The specific values of applied physical properties are presented in Table 2. The initial diameter of the water droplet D_0 is in the range of 20~100 μm and the velocity of uniform airflow U_g is in the range of

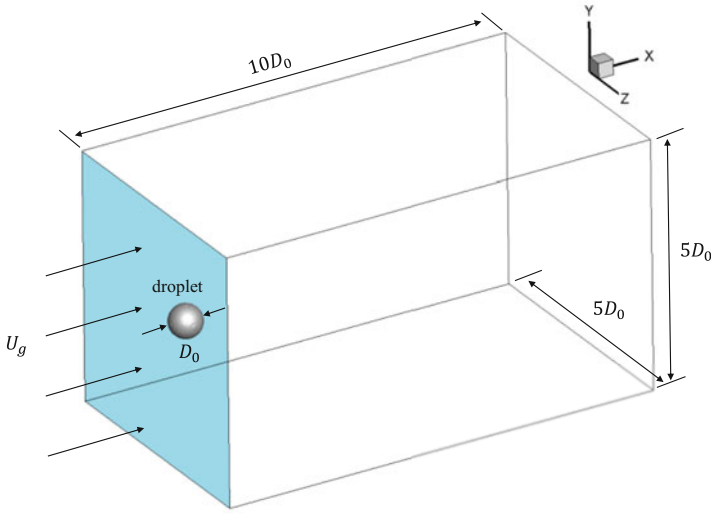

Fig. 11 Schematic illustration of the 3D computational domain

Table 2 Physical properties of water droplet and air phase used in numerical simulations

Temperature (°C)	ρ_l(kg/m^3)	ρ_g(kg/m^3)	μ_l(Pa · s)	μ_g(Pa · s)	σ(N · m)
−25	999	1.424	6.0×10^{-3}	1.59×10^{-5}	0.0793
25	997	1.185	0.898×10^{-3}	1.84×10^{-5}	0.0728

10~100 m/s. The simulated initial conditions, non-dimensional numbers, and outcomes in the present section are summarized in Table 3.

The deformation modes of the droplet are categorized into four regimes: vibration, transition, bag breakup, and bag-stamen breakup. The examples are presented in Fig. 12 for each deformation regime. In the present work, non-dimensional time is used and the definition is given as:

$$t^* = \frac{t}{\tau} = \frac{U_g}{D_0\sqrt{\rho_l/\rho_g}}t \tag{23}$$

As presented in Fig. 12a, the vibration mode is defined as the water droplet being able to maintain its initial spherical form during the whole computation, without obvious deformation. As shown in Fig. 12b, when the Weber number is increased, the droplet is in transition mode and remarkable deformation occurs. The droplet is elongated in cross-stream and streamwise directions alternately without fragmentations. For bag breakup mode shown in Fig. 12c, the water droplet first deforms into a staircase pyramid ($t^* = 0.5$). As the droplet is further compressed in a streamwise direction, it turns into disk form ($t^* = 1$) due to the strong aerodynamic force. Then

Table 3 Summary of investigated parameters and outcomes for different simulations

Case No.	*We*	*Re*	T(°C)	D_0(μm)	U_g(m/s)	Deformation mode
1	0.03	221.96	25	20	10	Vibration
2	0.13	443.92	25	20	20	Vibration
3	0.53	887.84	25	20	40	Vibration
4	2.11	1775.69	25	20	80	Transitional
5	0.08	554.90	25	50	10	Vibration
6	0.33	1109.80	25	50	20	Vibration
7	1.32	2219.61	25	50	40	Transitional
8	5.27	4439.22	25	50	80	Transitional
9	0.16	1109.80	25	100	10	Vibration
10	0.66	2219.61	25	100	20	Vibration
11	2.63	4439.22	25	100	40	Transitional
12	10.53	8878.44	25	100	80	Bag breakup
13	2.96	3329.41	25	50	60	Transitional
14	4.03	3884.32	25	50	70	Transitional
15	6.66	4994.12	25	50	90	Transitional
16	5.92	6658.83	25	100	60	Transitional
17	8.06	7768.63	25	100	70	Transitional
18	13.33	9988.24	25	100	90	Bag breakup
19	16.45	11098.05	25	100	100	Bag-stamen breakup
20	1.44	332.58	−25	50	40	Vibration
21	2.25	415.72	−25	50	50	Vibration
22	3.23	498.87	−25	50	60	Transitional
23	4.40	582.01	−25	50	70	Transitional
24	5.75	665.16	−25	50	80	Transitional
25	7.28	748.30	−25	50	90	Transitional
26	2.16	498.87	−25	75	40	Vibration
27	3.37	623.59	−25	75	50	Transitional
28	4.85	748.30	−25	75	60	Transitional
29	6.60	873.02	−25	75	70	Transitional
30	8.62	997.74	−25	75	80	Transitional
31	10.91	1122.45	−25	75	90	Bag breakup
32	2.87	665.16	−25	100	40	Vibration
33	4.49	831.45	−25	100	50	Transitional
34	6.47	997.74	−25	100	60	Transitional
35	8.80	1164.03	−25	100	70	Transitional
36	11.50	1330.32	−25	100	80	Bag breakup
37	14.55	1496.60	−25	100	90	Bag breakup

the liquid film is expanded along the streamwise direction and a thin hollow bag appears. Finally, a breakup occurs as the droplet is further accelerated by surrounding airflow. Bag-stamen breakup mode is observed with a higher *We* number as shown in Fig. 12d. Different from the bag breakup mode, in the center of the bag a

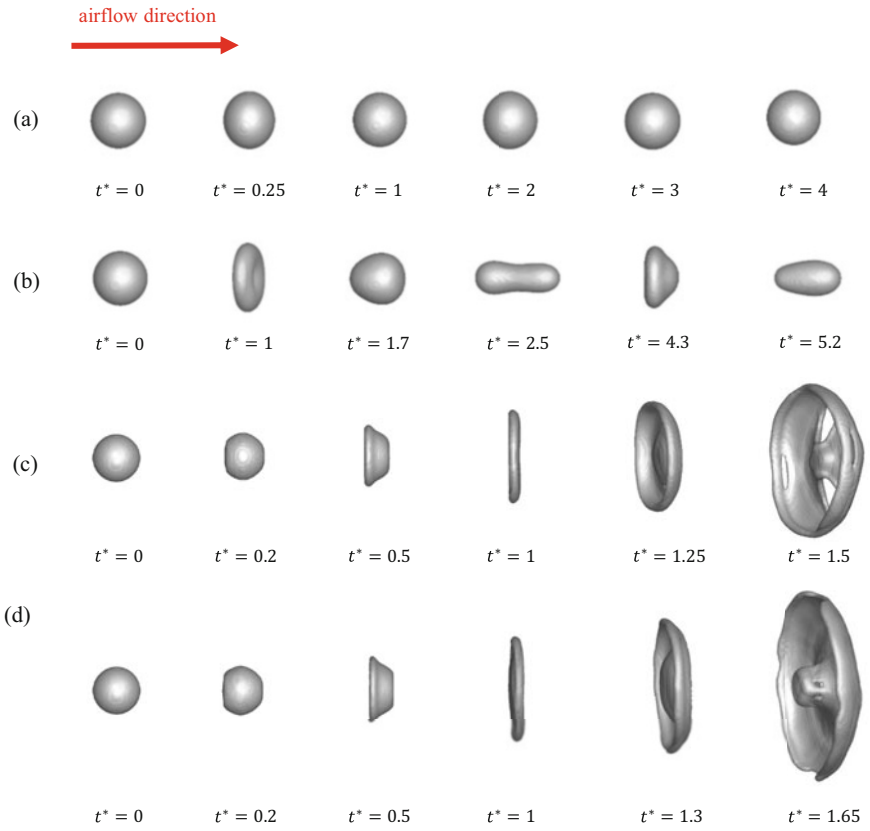

Fig. 12 Schematic of different deformation modes: (**a**) vibration mode (Case 3, $We = 0.53$), (**b**) transition mode (Case 15, $We = 6.66$), (**c**) bag breakup (Case 18, $We = 13.3$), (**d**) bag-stamen breakup (Case 19, $We = 16.5$)

thin stamen appears against the incoming flow. The whole simulated bag-stamen breakup process matches well with the experimental results for the case of $We = 18$ from Zhao et al. (2013).

Droplet Deformation and Breakup Regimes

To summarize the numerical outcomes presented in Table 3, the regime map of droplet deformation dependent on *We* number is presented in Fig. 13. It is shown that the deformation and breakup modes are dominated by the non-dimensional *We* number. When the parameter *We*is smaller than 1, the water droplet is in vibration mode. The initial spherical configuration is maintained, and no visible deformation appears during the movement. This value agrees well with the numerical works of Kékesi et al. (2014). When $1 < We < 10$, the water droplet turns into transition mode

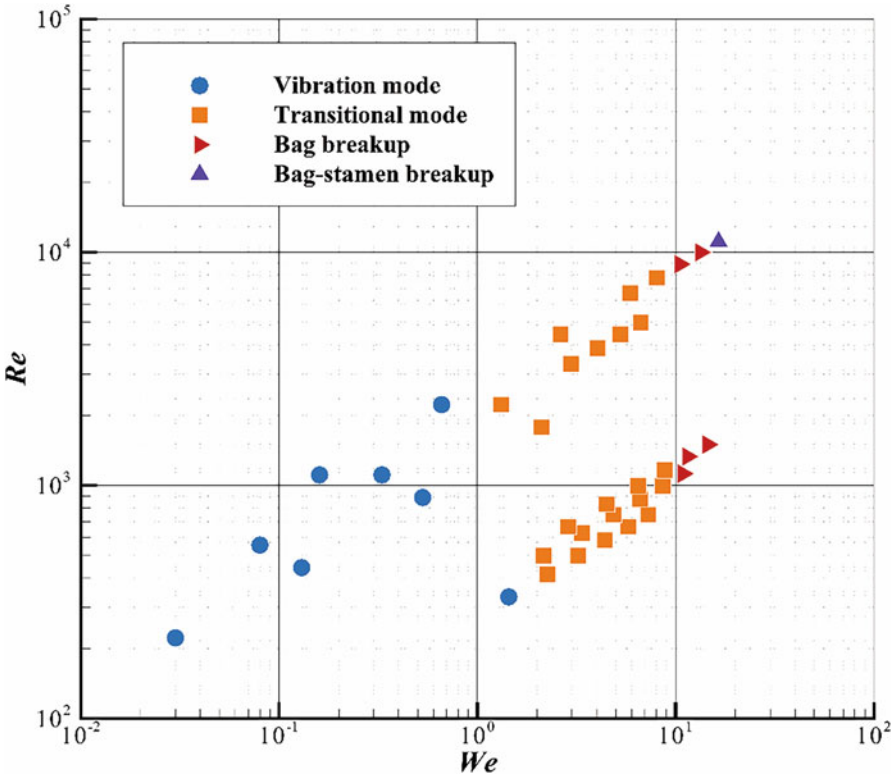

Fig. 13 Droplet deformation and breakup regimes for simulated cases

with significant deformations. When *We* is over the critical value of 10, a droplet is in bag breakup mode. As *We* becomes greater than 15, the droplet turns into bag-stamen breakup mode. This deformation regime map from the present numerical results has good agreement with the experimental works of Krzeczkowski (1980) and Guildenbecher et al. (Sojka and Guildenbecher 2011).

The non-dimensional Rayleigh-Taylor wave number N_{RT} was proposed by Zhao et al. (2010) as a critical condition of bag breakup. The fit correlation between the wave number N_{RT} and *We* number is given as:

$$N_{RT} = 0.076\left(1 + 0.19\mathrm{We}^{0.5}\right)^2\sqrt{1.2\mathrm{We}} \tag{24}$$

and droplet bag breakup mode occurs when $1/\sqrt{3} < N_{RT} < 1$. The simulated We number in the present investigation and the corresponding wave number N_{RT} are shown in Fig. 14. Since the deformation/bag breakup threshold is $N_{RT} = 1/\sqrt{3}$ (black dashed line), it is shown that the numerical results agree well with the conclusions of Zhao et al. (2010).

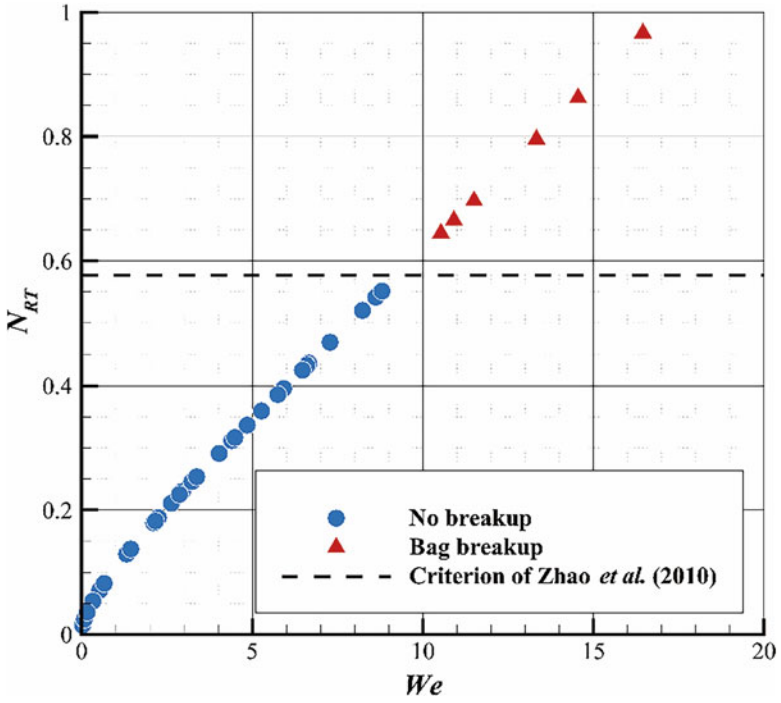

Fig. 14 Numerical results compared with the breakup criterion from Zhao et al. (2010)

Temporal Evolutions of Deformation Factor

The non-dimensional parameter named deformation factor (L) is defined to estimate the droplet deformation, following the work of Quan et al. (Quan and Schmidt 2006). It is the ratio between the cross-stream diameter and the streamwise diameter, $L = D_y/D_x$, as illustrated in Fig. 15.

The temporal evolutions of the deformation factor are given in Fig. 16 for droplet vibration mode. In the vibration regime, the aerodynamic force is small and the surface tension force of the droplet can maintain its original shape. As it is shown in Fig. 16 the deformation factor L varies between 1.0 and 1.1 during the acceleration process, which means the droplet remains spherical but slightly compressed in the stream-wise direction.

The temporal evolutions of the deformation factor are given in Fig. 17 for droplet transition mode. For better visibility, the numerical results of $T = 25$ °C are presented and grouped by initial droplet diameter. It is shown in Fig. 17 that in transition mode, the deformation factor L is in approximately periodical variation. Also, the peak values and period of deformation factor L become greater at a larger We number. This is consistent with the well-known conclusion that a greater Weber number results in a more dramatic deformation.

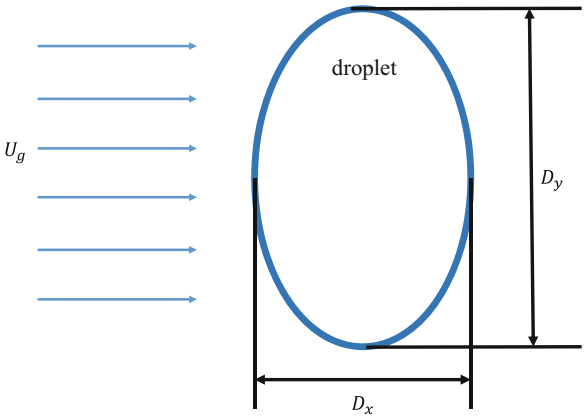

Fig. 15 Sketch of the deformed droplet and deformation factor

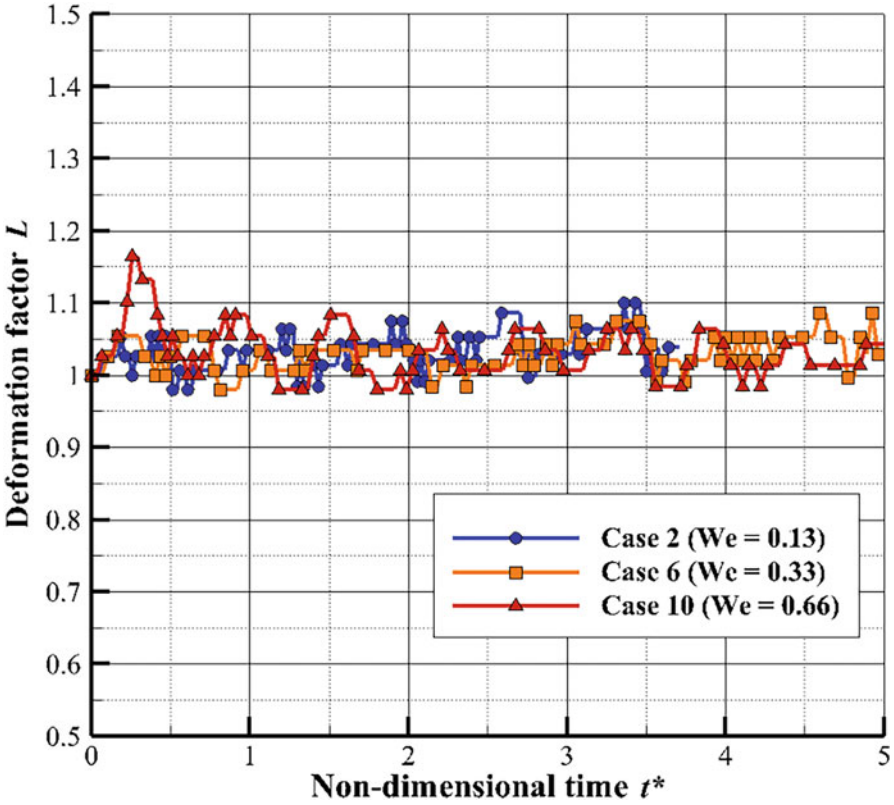

Fig. 16 Temporal evolutions of deformation factor of vibration mode

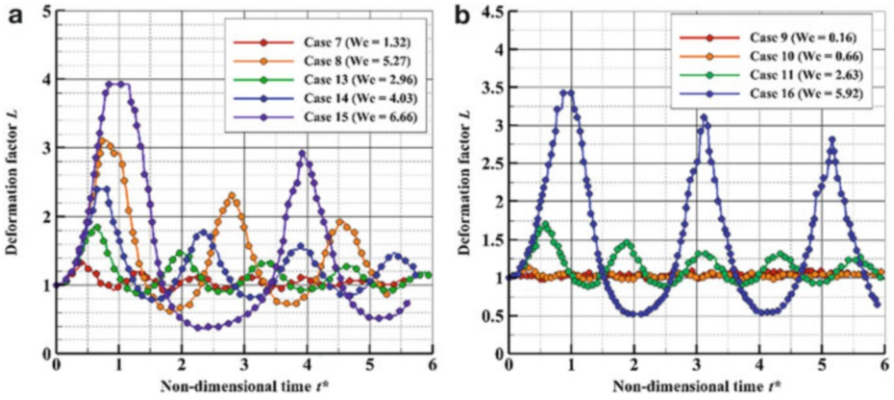

Fig. 17 Temporal evolutions of deformation factor of transition mode (**a**) $D_0 = 50$ μm, (**b**) $D_0 = 100$ μm

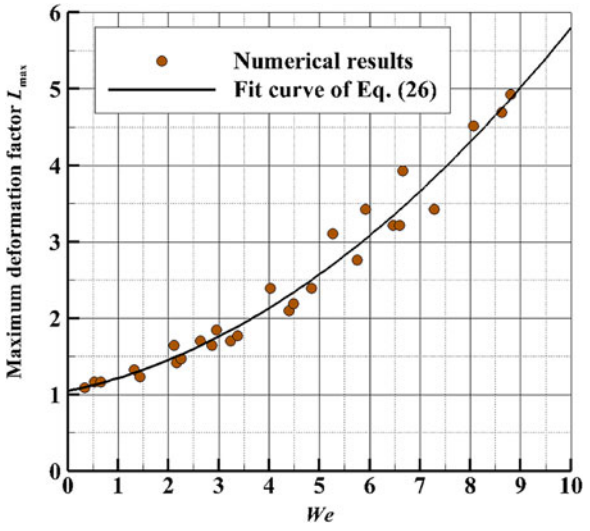

Fig. 18 The minimum deformation factor L_{max} of simulated transition mode

The maximum deformation factor L_{max} is a vital parameter in the study of liquid droplet deformation since it describes the extent of droplet deformation and the windward area of the deformed droplet. During its periodical movement, the droplet reaches the maximum deformation factor (maximum cross-stream diameter) at the first peak of the curves given in Fig. 17. The simulated L_{max} of each droplet transition case are shown in Fig. 18 against *We*. It is shown that the value of L_{max} increases with larger *We* , and the best fit correlation is given as:

$$L_{max} = 0.034We^2 + 0.135We + 1.048 \tag{25}$$

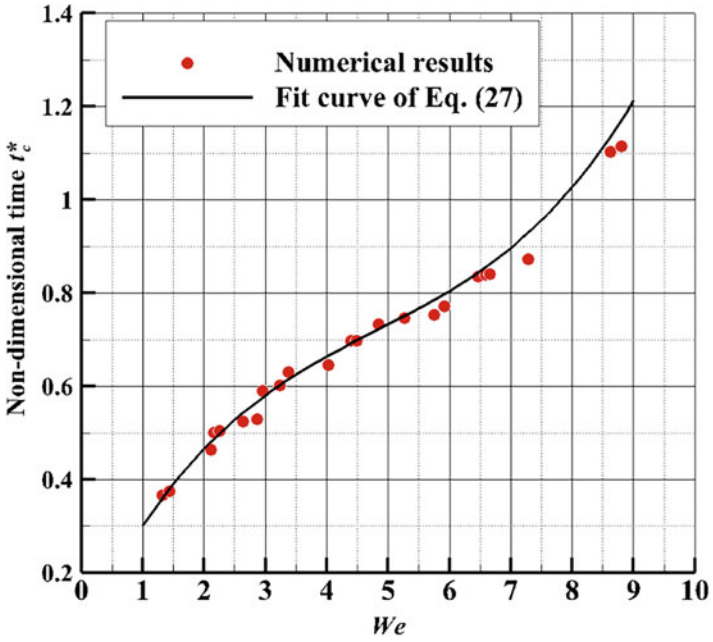

Fig. 19 The critical time t_c^* of minimum deformation factor

The critical time t_c^* to reach the maximum deformation factor L_{max} is also studied. The values of t_c^* against Weber number are shown in Fig. 19 for each transition case. It is shown that the value of t_c^* is increased along with the value of We. Since the droplet has a greater extent of deformation at higher We, it takes more non-dimensional time to reach its maximum cross-stream diameter. The best fit polynomial correlation for the critical time t_c^* is given as:

$$t_c^* = 0.03We(We - 11)^2 + 0.023(We - 2)^2 \tag{26}$$

During the droplet bag breakup process, the temporal evolution of cross-stream diameter D_c before breakup has been widely studied. Chou et al. (Chou and Faeth 1998) proposed their empirical correlation of D_c/D_0 as a function of non-dimensional time:

$$\frac{D_c}{D_0} = 1.0 + 0.5t^*, 0 \le t^* \le 2 \tag{27}$$

Cao et al. (2007) suggested the temporal evolution of D_c/D_0 as:

$$\frac{D_c}{D_0} = \begin{cases} 1.0, & 0 \le t^* \le 0.3 \\ 0.59 + 1.34t^*, & 0.3 \le t^* \le 0.99 \end{cases} \tag{28}$$

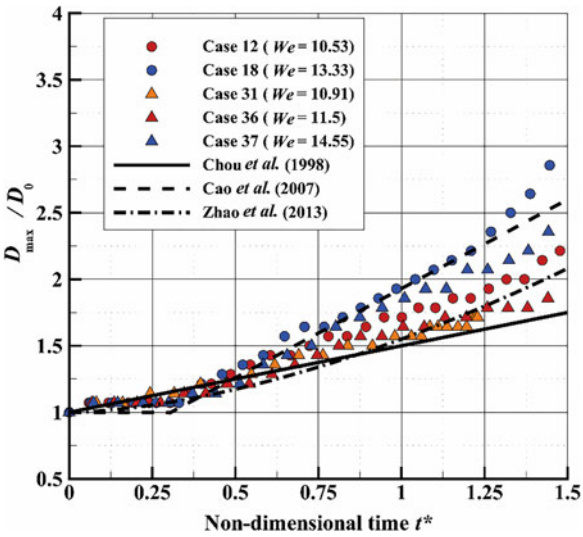

Fig. 20 The temporal evolutions of the cross-stream diameter of simulated bag breakup mode

and Zhao et al.(2013) proposed the function of D_c/D_0 as:

$$\frac{D_c}{D_0} = 1.0 + 0.54(t^*)^{1.67}, 0 \le t^* \le 1.5 \tag{29}$$

The simulated temporal evolutions of D_c/D_0 are presented in Fig. 20 for the droplet breakup regimes. It is shown that the numerical results agree well with the published conclusions. The numerical results have better consistency with the results of Cao et al. (2007) at higher *We*, while fitting better with the works of Chou et al. (Chou and Faeth 1998) and Zhao et al. (2013) at relatively smaller *We*.

Deformation and Breakup Mechanism Analysis

The droplet's velocity and pressure distributions are analyzed for investigating the mechanisms of droplet deformation and breakup. The temporal evolutions of *x*-component velocity and pressure fields are presented in Fig. 21 for case 20, where the droplet is in a vibration regime. It is found in Fig. 21a that at the beginning of acceleration ($t^* = 0.5$), due to the existence of the droplet, the uniform airflow passes around the droplet and a stagnation point occurs at the windward side of the droplet. At the same time, a pair of symmetric vortices are generated behind the droplet. As shown in Fig. 21b, the high-pressure region appears at the windward side of the droplet, while the low-pressure region appears at the downstream region. This non-uniform pressure distribution leads to the deformation that the droplet is compressed in the airflow direction. As the flow further develops, the pressure difference between the windward and leeward sides of the droplet decreases, as well as the scale of the circulation. In the vibration regime, *We* is small and the surface tension force of the droplet can balance the aerodynamic force and viscous

force so that the spherical shape of the droplet is maintained during the acceleration process.

The temporal evolutions of x-component velocity and pressure fields are presented in Fig. 22 for case 20, in which the droplet is in a transition regime. It is seen in Fig. 22 that due to the strong effect of aerodynamic force, a low-pressure area is generated at the downstream area ($t^* = 0.9$). The produced pressure difference elongates the water droplet in the cross-stream direction and turns it into a disk shape. Meanwhile, a pair of symmetric vortexes are generated at the downstream region. In this circumstance, the surface tension force can still retain the whole interface, and the droplet turns back into a spherical shape. At $t^* = 2.5$, the droplet deforms into an ellipsoid with minimum

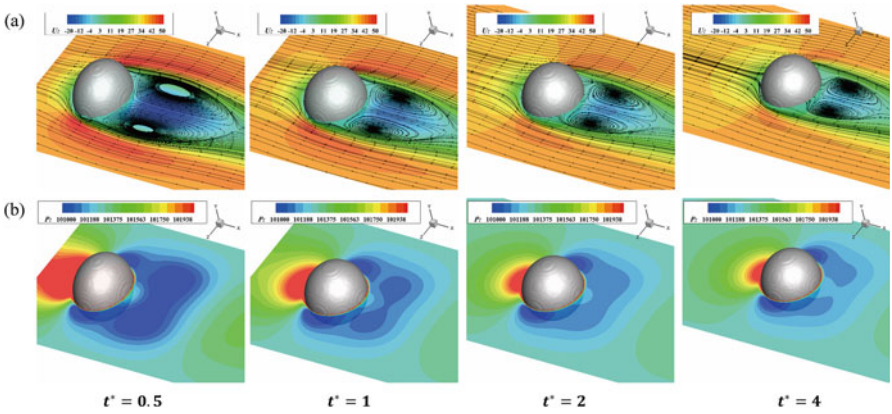

Fig. 21 Temporal evolutions of droplet configuration (case 20) (**a**) x-component velocity field, (**b**) pressure field

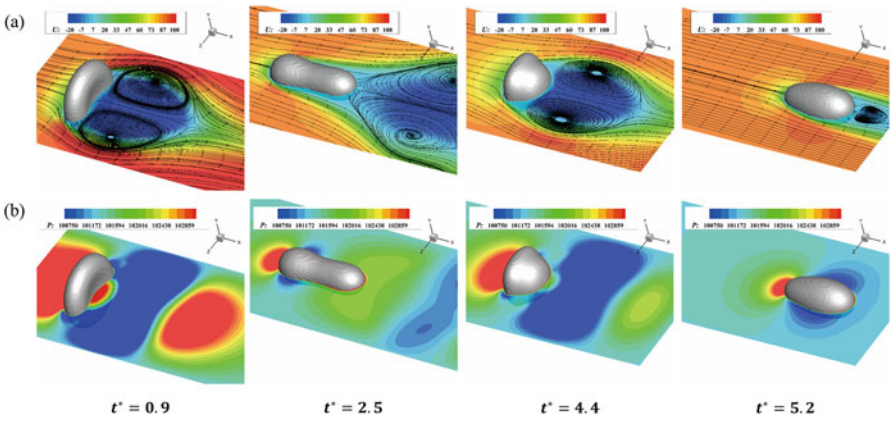

Fig. 22 Temporal evolutions of droplet configuration (case 15) (**a**) x-component velocity field, (**b**) pressure field

cross-stream diameter. The detour of airflow is alleviated, and the symmetric vortex starts to separate from the droplet. During the following movement, the deformation of the droplet is approximately periodical.

The temporal evolutions of x-component velocity and pressure fields are presented in Fig. 23 for case 20, where the droplet is in the breakup regime. As the acceleration is trigged, the symmetric vortex pair is generated at the downstream region and the recirculation keeps growing more prominent. By contrast to the situations of vibration and transition regimes, the pressure difference around the droplet keeps increasing, and the airflow at the downstream area becomes turbulent. During the development, the droplet is further flattened by the recirculation and continuously stretched in the cross-stream direction. The details of the flow field near the droplet are given in Fig. 24 for moment $t^* = 0.55$ an $t^* = 1.2$. The structures

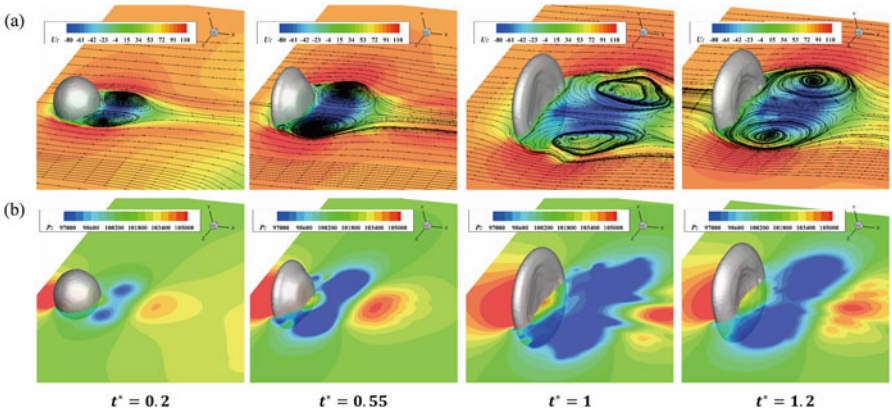

Fig. 23 Temporal evolutions of droplet configuration (case 18) (**a**) x-component velocity field, (**b**) pressure field

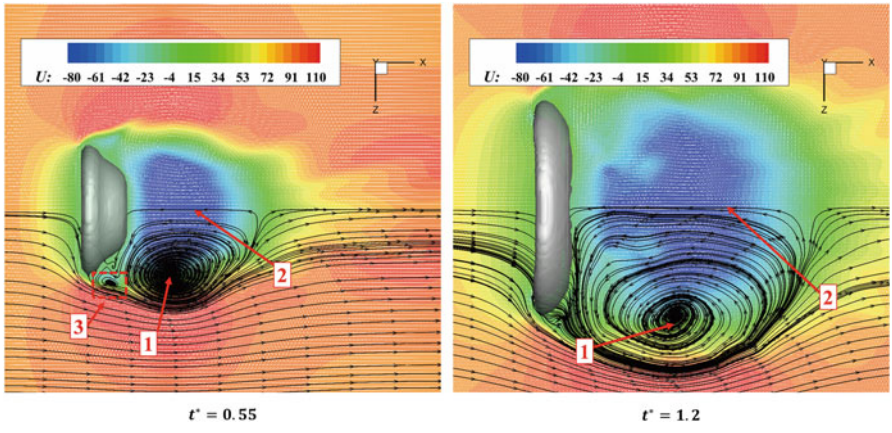

Fig. 24 Details of the flow field near the droplet (case 18)

1-toroidal vortex pair in the flow separation region and 2-return flow near the wake axis are identified in Fig. 24, which are observed in vibration and transition regimes as well. At $t^* = 0.55$, the droplet deforms into a staircase pyramid, and a structure 3-solitary toroidal vortex appears near the rim of the droplet. The vortex keeps developing, and the recirculation region is further expanded. In this circumstance, the surface tension force cannot overcome the effect of aerodynamic force and, finally, droplet breakup occurs.

Effect of Water Droplet Supercooling

In aircraft icing problems, the water droplets encountered by aircraft are usually in a supercooled state. To investigate the effect of supercooling on water droplet deformation, comparisons between numerical results under different temperatures are presented in Fig. 25. It is shown that with the same initial diameter and airflow velocity, the deformation factor is decreased compared with the results at room temperature. Also, the variation becomes larger at higher *We* numbers. As it is shown in Table 2 for the supercooled state, the water droplet viscosity significantly increases compared to room temperature, while the surface tension coefficient slightly changes. Due to a larger internal viscous force of supercooled water droplets, the effect of aerodynamic force is withstood, and the droplet deformation is attenuated. In Fig. 25 it is worth noting that for each airflow velocity, the curves of different temperatures have similar tendencies till the droplet reaches its maximum deformation factor.

Conclusions

Firstly, a systemic numerical method is proposed for solving incompressible multiphase flow problems. In which, the continuity and momentum equations are solved with the projection method, the transport and reinitialization equations of level-set function ϕ are solved to capture the liquid-air interface, the governing equations are discretized and solved within a staggered grid system, and the adaptive time step that determined by convection, viscosity, and surface tension is used to meet CFL criterion. Three typical multiphase flow problems (Rayleigh-Taylor instability, water droplet splashing on a thin water film, and water column collapsing problem) are simulated via introduced numerical methods. The accuracy of the adopted numerical methods is validated by the excellent agreement between the present numerical results of classical multiphase flow problems and the published results.

Secondly, the water droplet deformation in continuous airflow is numerically studied in the present section. The microscale water droplet with initial diameter $D_0 = 20\sim100$ μm, and the uniform airflow with velocity $U_g = 10\sim100$ m/s, are simulated according to the conventional environment conditions of aircraft icing problems. The numerical results indicate that the droplet is in vibration mode, and it can retain the initial spherical shape when $We < 1$. For $We < 10$ the droplet is in a transition mode, where periodical deformations are observed. As *We* is greater than the critical value 10, the droplet is in bag breakup mode. Additionally, the phase

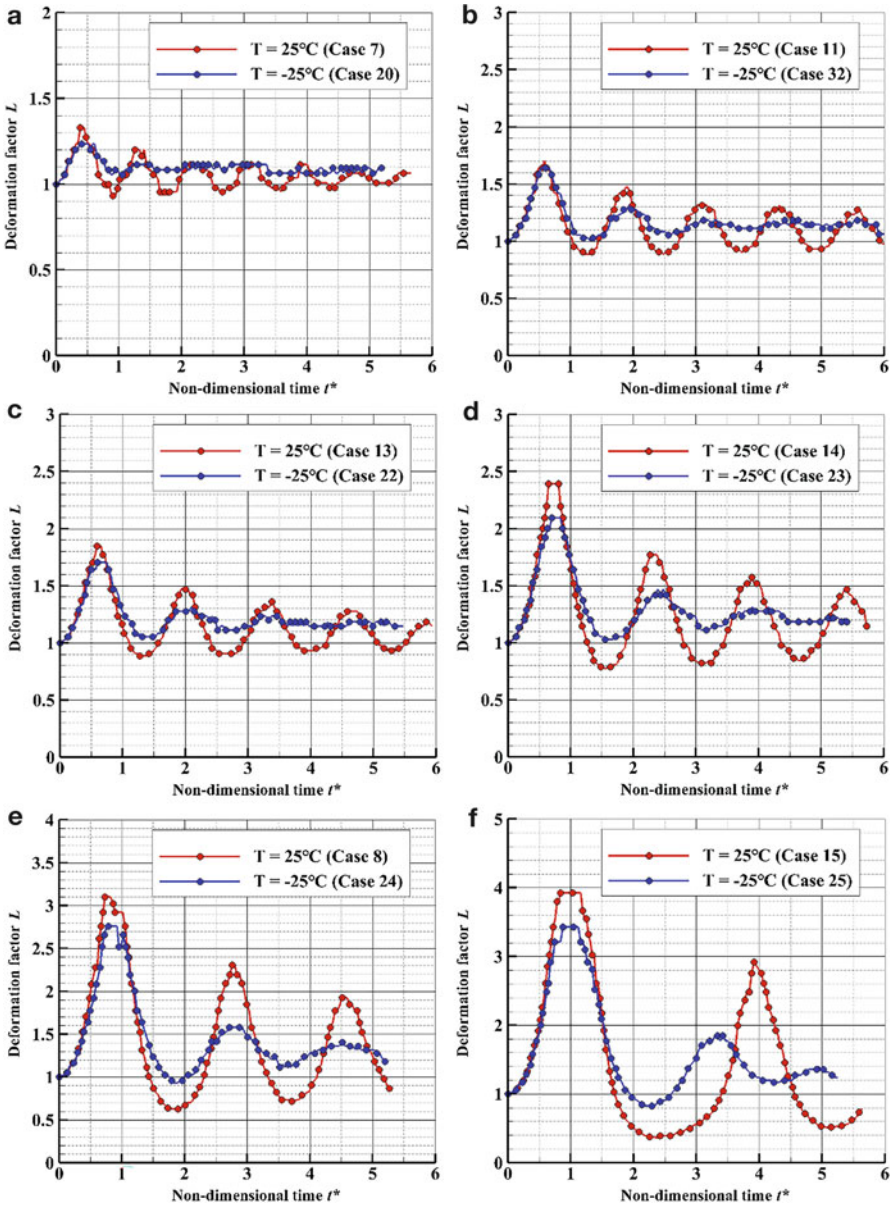

Fig. 25 Temporal evolutions of deformation factor (**a**) $D_0 = 50$ μm, $U_g = 40$ m/s, (**b**) $D_0 = 100$ μm, $U_g = 40$ m/s, (**c**) $D_0 = 50$ μm, $U_g = 60$ m/s, (**d**) $D_0 = 50$ μm, $U_g = 70$ m/s, (**e**) $D_0 = 50$ μm, $U_g = 80$ m/s, (**f**) $D_0 = 50$ μm, $U_g = 90$ m/s

properties corresponding to a low temperature $T = -25$ °C are tested to study the supercooling effects on droplet deformation. The numerical results reveal that with the same initial droplet diameter D_0 and uniform airflow velocity U_g the extent of

deformation is decreased for supercooled water droplets compared to the results with room temperature. Such quantitative analysis results could help with understanding the physical intrinsic characteristic behind the droplet deformation phenomenon.

Droplet Impact on Surfaces with Different Hydrophobicity

In this section, both the level-set and the Lattice Boltzmann methods are employed to investigate the droplet impingement on surfaces with different hydrophobicity. Since the level-set methodology is presented above, only a description of the Lattice Boltzmann method is given below.

Pseudopotential Lattice Boltzmann Method and Curved Boundary Treatment

Due to the advantages of the Lattice Boltzmann method in dealing with curved surface boundaries, a three-dimensional nineteen-velocity (D3Q19) pseudopotential multiphase Lattice Boltzmann model based on multiple-relaxation-time (MRT) collision operator is applied to investigate the droplet impact on a superhydrophobic surface with protrusions, which can be expressed as:

$$f_i(x + e_i\delta t, t + \delta t) - f_i(x, t) = -M^{-1}SM\left(f_i(x, t) - f_i^{eq}(x, t)\right) + \Delta f_i \tag{30}$$

where $f_i(x, t)$ is the particle distribution function, e_i is the particle velocity in the ith direction, M is a transformation matrix, S is a diagonal matrix, $f_i^{eq}(x,t)$ is the equilibrium distribution function, and the exact difference method (EDM) (Kupershtokh et al. 2009) is adopted which is corresponding to the third term on the right side of the equation.

For the D3Q19 model, the discrete lattice velocity e_i is given as:

$$e_i = \begin{cases} (0,0,0) & i = 0 \\ (\pm 1,0,0)(0,\pm 1,0)(0,0,\pm 1) & i = 1,\cdots,6 \\ (\pm 1,\pm 1,0)(\pm 1,0,\pm 1)(0,\pm 1,\pm 1) & i = 7,\cdots,18 \end{cases} \tag{31}$$

and $f_i^{eq}(x,t)$ can be expressed as:

$$f_i^{eq} = w_i\rho\left(1 + \frac{e_i \cdot u}{c_s^2} + \frac{(e_i \cdot u)^2}{2c_s^4} - \frac{u \cdot u}{2c_s^2}\right) \tag{32}$$

where $w_0 = 1/3$, $w_{1\ -\ 6} = 1/18$, $w_{7\ -\ 18} = 1/36$, and $c_s^2 = c^2/3$ with $c = \delta_x/\delta_t$. The density ρ and velocity u can be obtained by the following relationships:

$$\begin{aligned}\rho &= \sum_{i=0}^{18} f_i \\ \rho u &= \sum_{i=0}^{18} e_i f_i\end{aligned} \tag{33}$$

Using the transformation matrix M, the whole particle evolution can be divided into the following two steps:

$$m^* = m - S(m - m^{eq}) \tag{34}$$

$$f_i(x + e_i\delta t, t + \delta t) = f_i^*(x, t) + \Delta f_i \tag{35}$$

where $m = Mf$, $m^{eq} = Mf^{eq}$, $f^*(x, t) = M^{-1}m^*$, and Δf_i is the force term which can be explicitly expressed as $\Delta f_i = f_i^{eq}(\rho, u + \Delta u) - f_i^{eq}(\rho, u)$ where $\Delta u = F\delta t/\rho$ and the actual macroscopic velocity is $\rho v = \sum_{i=0}^{18} e_i f_i + F\delta t/2$ (Kupershtokh et al. 2009).

In the pseudopotential multiphase model, the intermolecular interaction force is introduced to achieve phase separation which is given as:

$$F_{int} = \beta \sum Gw_i\phi^2(x + e_i)e_i + (1 - 2\beta)\phi(x) \sum Gw_i\phi(x + e_i)e_i \tag{36}$$

where β is fixed at 0.152, G equals 3, and $\phi = \sqrt{\overline{\rho}c_s^2 - k\overline{p}}$, where $\overline{p} = p/p_c$, $\overline{\rho} = \rho/\rho_c$, and $k = 0.01$. Due to its remarkable performance in high density ratio simulations, the reduced formulation of Carnahan-Starling EOS is applied, which reads:

$$\overline{p} = 2.7859\overline{\rho}\overline{T}\frac{1 + \frac{0.13044\overline{\rho}}{4} + \left(\frac{0.13044\overline{\rho}}{4}\right)^2 - \left(1 - \frac{0.13044\overline{\rho}}{4}\right)^3}{\left(1 - \frac{0.13044\overline{\rho}}{4}\right)^3} - 3.8525\overline{\rho}^2 \tag{37}$$

To mimic the wet phenomenon, the adhesive force between the fluid and the solid wall is introduced which is computed by (Li et al. 2014):

$$F_{ads} = -G_{ads}\phi(x) \sum_{i=0}^{19} w_i\phi(x)s(x + e_i)e_i \tag{38}$$

where G_{ads} is used to adjust the wettability and $s(x + e_i)$ is an indicator function which is equal to 1 for solid and 0 for fluid. The gravitational force is given as:

$$F_g = \rho g \tag{39}$$

Where g is the gravitational acceleration. To obtain a stable initial density field, the droplet is equilibrated after 10,000 times without gravity, and the initial velocity of

the droplet is added by the second law of Newton. Therefore, the specific form of gravity becomes:

$$F_g = \begin{cases} 0 & time < 10000 \\ \widehat{\rho}\frac{v_{int}}{\delta t} & time = 10000 \\ \rho g & time > 10000 \end{cases} \qquad \widehat{\rho} = \begin{cases} 0 & \rho < \rho_{avg} \\ \rho & \rho \geq \rho_{avg} \end{cases} \tag{40}$$

Where ρ_{avg} is the average density in the computational domain.

In the LB community, the bounce-back scheme is widely applied for non-slip boundaries due to its simplicity. However, it will cause staircase approximation of curved walls, which loses the fidelity of real geometry and introduces additional errors. Furthermore, most of LBM's common curved boundary schemes have a mass leakage problem. In the present work, an improved scheme is proposed based on the halfway bounce-back interpolation boundary condition (HBI) scheme (Ling et al. 2020). The unknown distribution function in the HBI scheme can be expressed as:

$$f_{-i}(x_f, t + \Delta t) = \overline{f}_i(x_f, t) + \frac{2q-1}{2q+1}\left(\overline{f_{-i}}(x_f, t) - \overline{f}_i(x_{ff}, t)\right) \tag{41}$$

Where $x_{ff} = x_f - e_i\Delta t$ and $q = \frac{|x_f - x_w|}{|x_f - x_s|}$ as illustrated in Fig. 26. To avoid the negative f_0 and overcome the mass leakage problem, the leakage mass is added to all the distributions of the particular fluid node, multiplied by the corresponding weights following the idea of Sanjeevi (Sanjeevi et al. 2018). It should be noted that the corrections should be carried out after the force measurement, because the actual

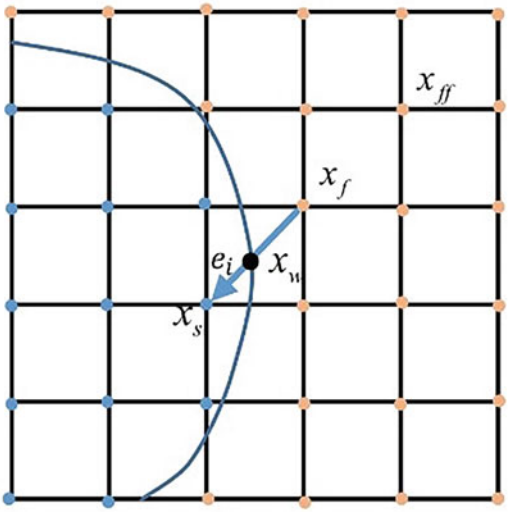

Fig. 26 Schematic of a curved wall immersed in the fluid region (blue point: solid node, orange point: fluid node, blue line: curved boundary)

force on the particle would be corrupted by these corrections (Sanjeevi et al. 2018). The mass leakage at the curved wall boundary can be computed as (Yu et al. 2020):

$$\Delta m\left(x_f, t+\Delta t\right) = \sum_{outgoing} \overline{f_i}\left(x_f, t\right) - \sum_{incoming} \overline{f_{\bar{i}}}\left(x_f, t+\delta t\right) \tag{42}$$

Then, the final formulations of distribution functions at the boundary node can be expressed as:

$$f_i^{\text{final}} = f_i + w_i \Delta m \tag{43}$$

It needs to be noted that the droplet will undergo non-physical deformation and "evaporation" without mass-conservation corrections, which have been reported in (Yu et al. 2020). In addition, the strategies proposed by Wu et al. (2018) are employed to improve the simulation stability.

In the Lattice Boltzmann method, the simulation parameters are all based on the lattice units, which are combinations of the basic units consisting of *mu* (Mass), *lu* (Length), *ts* (Time), and *tu* (Temperature), etc. For example, velocity is given in *lu*/*ts*, density in mu/lu^3, surface tension inmu/ts^2. A transformation relationship between lattice and real physical units can be established according to dimensional analysis. At the condition of $[oh]_{lu} = [oh]_{real}$, the transformation relationship between the units of length can be written as: $l_0 = \left[\frac{v_l^2 \rho_l}{\sigma}\right]_{real} / \left[\frac{v_l^2 \rho_l}{\sigma}\right]_{lu}$ where $[v_l]_{lu}$ is the liquid kinematic viscosity in LBM, $[\sigma]_{lu}$ is the surface tension in LBM which is 0.134 in our simulations according to Laplace's law and $[\rho_l]_{lu}$ is the liquid density in LBM. In the same way, at the condition of $[t_c]_{lu} = [t_c]_{real}$, the time scale can be obtained as: $t_0 = l_0^{1.5} \frac{\left[\left(\frac{\rho_l}{\sigma}\right)^{0.5}\right]_{real}}{\left[\left(\frac{\rho_l}{\sigma}\right)^{0.5}\right]_{lu}}$.

Validation of Related Numerical Methods

Before this study, method validations are highly required. Firstly, to validate the accuracy of the level-set method introduced in section "Governing Equations and Numerical Methods" in detail, an experiment about droplet impact on a super-hydrophobic surface was conducted, and the experimental results were compared with numerical results. Figure 27 illustrates the corresponding experimental setup. The water droplets are carefully released from the microliter syringe with a diameter range $D_0 = 2$~3.5 mm. The impact velocity of the water droplet is controlled in a range of $U_0 = 0$~3 m/s by adjusting the droplet release height. Poly tetra fluoro ethylene (PTFE) particles are adopted as the raw material of the homemade superhydrophobic coating. Firstly, the PTFE is mixed with ethanol and dispersed by a magnetic stirrer and ultrasonic cell disruptor. Then to improve stability, the thermosetting epoxy resin is added. The produced coating is sprayed on an aluminum plate, and the plate is

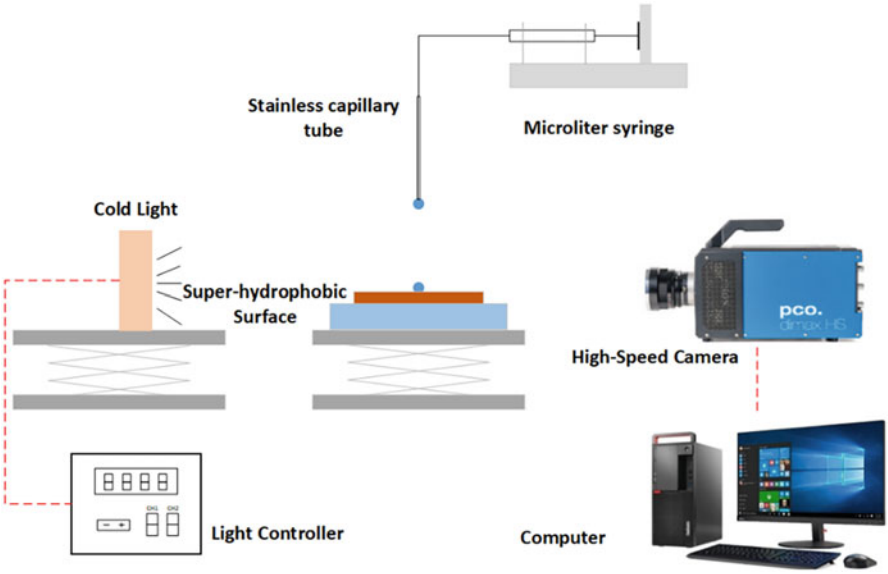

Fig. 27 Schematic of the experimental setup for droplet impact

soaked at a temperature of 80 °C for two hours to deposit a low-surface-energy monolayer. The equilibrium apparent contact angle for water droplets in the prepared surface is 156 ° ± 1° which is measured by the contact angle analyzer (SEO Phoenix 300 Touch, China). A high-speed camera PCO DLMAX HS4 is used to record the process of droplet impingement. The experiment with $D_0 = 2.14$ mm and $U_0 = 0.64$ m/s is implemented for the validation of the numerical method.

The set of level-set simulations is consistent with that of experiments and the properties of the liquid and gas phases are set as $\rho_l = 998\ kg/m^3$, $\rho_g = 1.185 kg/m^3$ for density, $\mu_l = 8.98 \times 10^{-4}\ Pa \cdot s$, $\mu_g = 1.84 \times 10^{-5}\ Pa\ s$ for viscosity and the liquid surface tension coefficient $\sigma = 0.0728$ N/m.

Figure 28 compares the water droplet deformations during the spreading and recoiling stages. Predictions of droplet topology from the numerical model agree well with the experimental results. In the initial phase, when the droplet contacts the solid surface, it becomes a truncated sphere. After that, the droplet expands into a pancake shape and reaches the maximum spreading factor. In the recoiling stage, the wetting area decreases with the height increase of the droplet center. In the end, the droplets rebound off the superhydrophobic solid surface.

As shown in Fig. 29, the non-dimensional parameter spreading factor ξ, which is defined as $\xi(t) = \frac{D(t)}{D_0}$, is compared. The time is nondimensionalized by

$$t^* = \frac{Ut}{D_0} \tag{44}$$

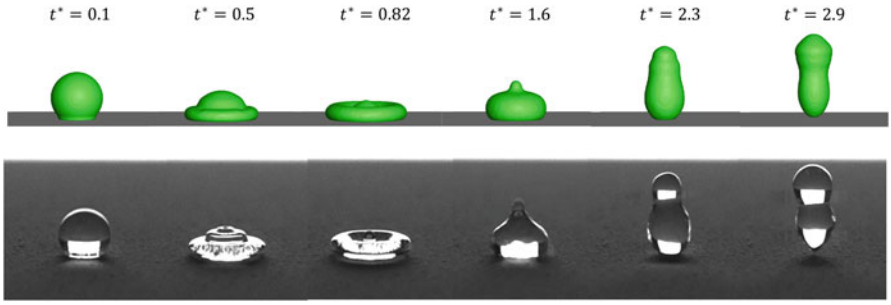

Fig. 28 Comparison of the droplet impact behaviors. Top: simulation results. Bottom: experimental results ($U_0 = 0.64\ m/s$, $D_0 = 2.14$ mm)

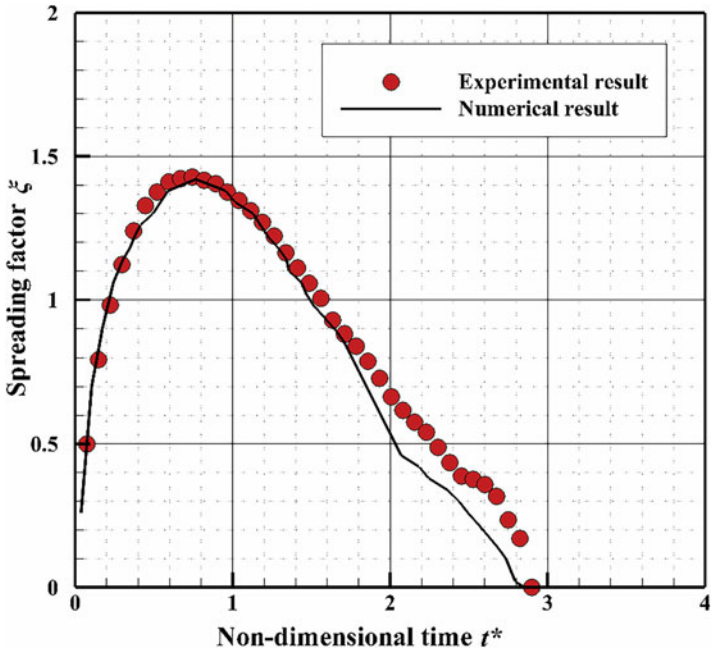

Fig. 29 Comparison of wetted surface diameter between the simulation and experiment. ($D_0 = 2.14$mm, $U = 0.64$m/s).

It can be found that the numerical results match well with the experimental results. In addition, the deviation in the maximum spreading factor between the numerical results ($\xi_{max} = 1.42$) and the experimental results ($\xi_{max} = 1.428$) is only 0.56%.

On the other hand, the reliability and accuracy of the three-dimensional pseudo-potential LBM are also validated before using it to investigate the droplet impact problem. Laplace's law is tested at first, with the computational domain set as $151 \times 151 \times 151\ lu^3$ with a periodic boundary condition at all side boundaries. Several

cases having a droplet with different radii from $R = 20$ *lu to* 40 *lu* initially located at the center of the domain are performed to obtain pressure difference inside and outside the droplet. In addition, for numerical stability, the diffuser density field is initialized as $\rho = \frac{\rho_l+\rho_g}{2} - \frac{\rho_l-\rho_g}{2}\tanh\left\{\frac{2\left[\sqrt{(x-x_0)^2+(y-y_0)^2+(z-z_0)^2}-R_0\right]}{W}\right\}$, where $W = 5$ *lu* is the initial interface thickness, R_0 is the initial droplet radius, and x_0, y_0 and z_0 are the initial center of the droplet which is also set as the center of the computational domain. The interface of the steady droplet is set as the location of the mean density $0.5(\rho_l + \rho_v)$, which is also used to measure the steady-state radius. It is worth noting that when the droplet reaches a stable state, its radius has a slight change compared with the initial radius due to the evolution of the interface. For a three-dimensional static droplet, Laplace's law can be expressed as:

$$\Delta p = p_{in} - p_{out} = \frac{2\sigma}{R} \tag{45}$$

where σ is the surface tension, R is the radius of the droplet, and p_{in} and p_{out} are the pressures inside and outside the droplet respectively. According to Laplace's law, the pressure difference should be proportional to the reciprocal of the droplet radius with constant surface tension. Figure 30 plots the change of pressure difference with the reciprocal of droplet radius. It can be found that the simulations agree well with the linear fit, which means that Laplace's law is well-validated.

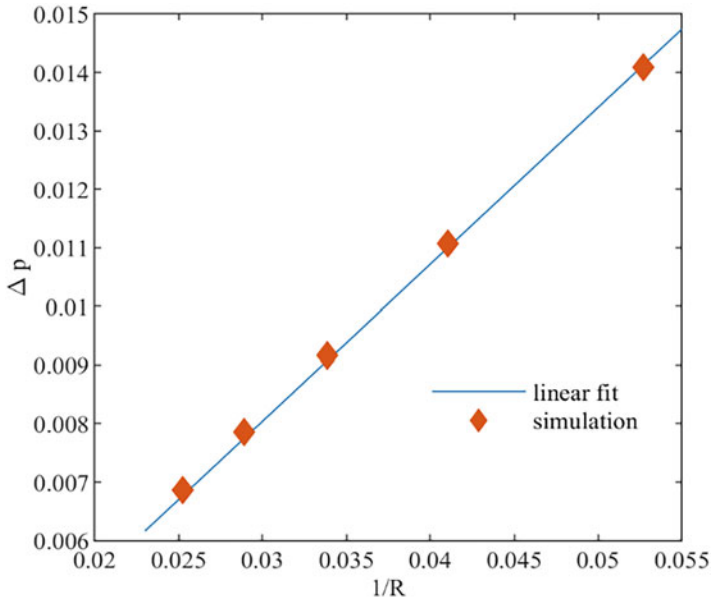

Fig. 30 Numerical verification of Laplace's law

In the thermodynamic theory, the thermodynamic coexistence curves (ρ_l and ρ_g) are determined by the Maxwell equal-area which is built in terms of the following requirement: $\int_{\rho_g}^{\rho_l} (P_0 - P_{EOS}) \frac{1}{\rho^2} d\rho = 0$, where P_{EOS} is the equation of state in thermodynamic theory and $P_0 = P_{EOS}(\rho_l) = P_{EOS}(\rho_g)$. For the original pseudopotential LB model, the gas-liquid two-phase density of the numerical solution in the pseudopotential LB model is different compared to the solution given by the Maxwell construction, especially when the two-phase density ratio is large. This problem is usually called thermodynamic inconsistency. In the present work, we employ the model proposed by Kupershtokh et al. (2009) to resolve the problem of thermodynamic inconsistency, which means adjusting β in Eq. (36) to make the numerical coexistence curves consistent with Maxwell constructions. To validate the thermodynamic consistency of our methods, serval cases about the one-dimensional flat interface are performed. Here, a three-dimensional domain with dimensions of $26 \times 26 \times 101$ is adopted, where the periodic boundary conditions are applied in both directions. To improve the numerical stability, the initial density profile is given by:

$$\rho = \frac{\rho_l + \rho_g}{2} - \frac{\rho_l - \rho_g}{2} \tanh\left(\frac{(|z - z_{center}| - r_0)}{W}\right) \tag{46}$$

where ρ_l and ρ_g are liquid density and gas density respectively, $W = 5$, $z_{center} = 50$ and $r_0 = 25$. As shown in Fig. 31, the numerical coexistence curves predicted by our methods are presented. For comparison, the results obtained with Maxwell's equal-area rule are also presented in Fig. 31, which refers to the black line. It can be seen that our results are in excellent agreement with the Maxwell construction in both the liquid and gas branches and even at $\overline{T} = 0.49$, which corresponds to $\frac{\rho_l}{\rho_g} = 875$, the

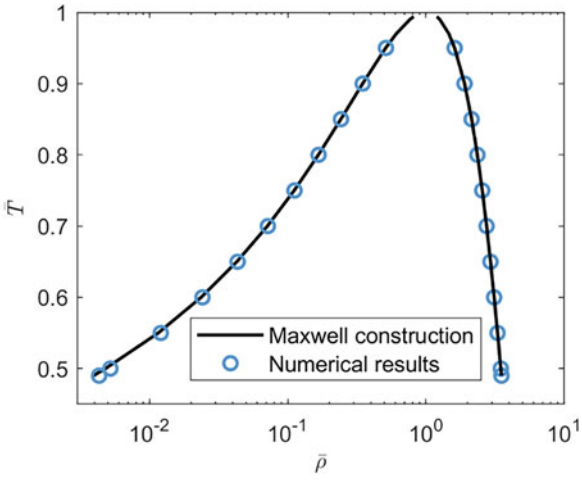

Fig. 31 Comparison of the numerical results with the analytical solution of the Maxwell construction

present method still works well, which means its thermodynamic consistency has been well validated.

Additionally, to assess the performance of the Lattice Boltzmann method, the droplet impact on a flat superhydrophobic surface is also validated with the experimental results (Li and Zhang 2019; Chen et al. 2011; Abolghasemibizaki and Mohammadi 2018). As shown in Fig. 32a, at $We = 2.64$, albeit of some deviation in time, the multi-layered pancake shape (at 1.4 ms) and the elongated droplet due to the non-uniform velocity distribution (at 9.8 ms) are all reproduced in simulations and agree well with the experiment. The droplet deformation after impacting a flat surface at $We = 10$ and 51.6 is shown in Fig. 32b and c, respectively. Good agreement with the experiment, in terms of droplet deformation and bouncing timing, can be achieved based on the present model. Therefore, it can be considered

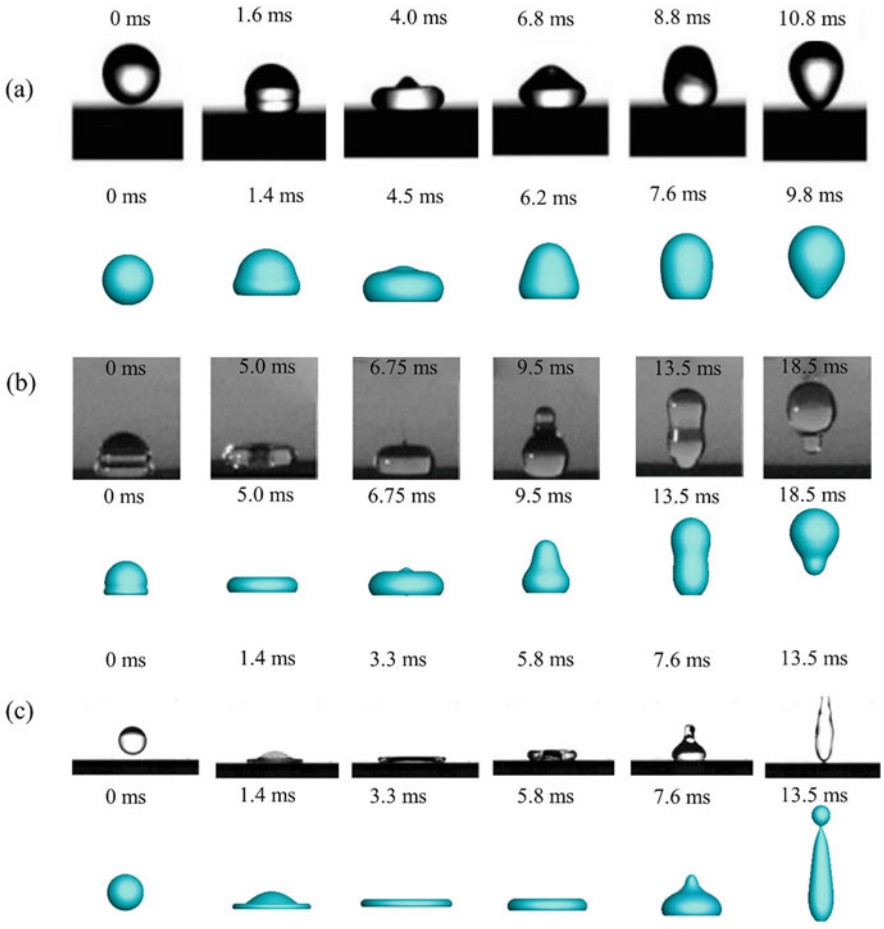

Fig. 32 Comparison of experimental and numerical results (**a**) $We = 2.64$ (Li and Zhang 2019), (**b**) $We = 10$ (Chen et al. 2011), (**c**) $We = 51.6$ (Abolghasemibizaki and Mohammadi 2018)

that the current methodology can reproduce the droplet impact dynamics faithfully for various values of the parameter *We*.

Results and Discussions

Droplet Impact on Flat Superhydrophobic Surfaces

The level-set method is applied to investigate microscale water droplets' impact on a superhydrophobic solid surface under various conditions. The simulations in this section are performed in a 3D domain with the dimensions of $4D \times 5D \times 4D$ as shown in Fig. 33. The grid resolution is 50 grids per droplet diameter. It has been proved that the present size of the domain is large enough to capture the droplet spreading and rebound movements. The solid bottom surface is set as a no-slip boundary condition, while other surfaces are specified as the pressure outlet boundary conditions. The intrinsic contact angle is defined as 156° for the wettability of a solid surface which is consistent with the experiment setup.

Taking the effects of temperature on droplet impact into consideration, different phase properties corresponding to temperatures from −25 °C to 25 °C are adopted. For the temperature below 0 °C , the water droplet is considered as a supercooled

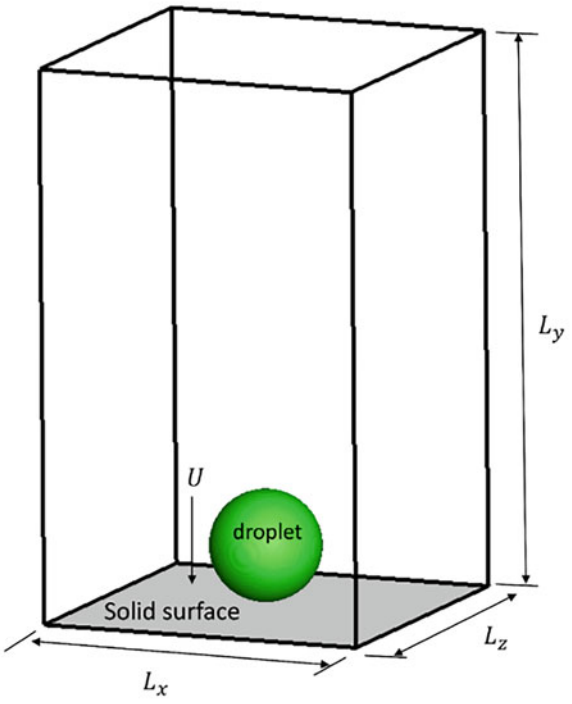

Fig. 33 Schematic illustration of the computational domain

state, and the solid-liquid phase change is not considered in the present numerical study. The specific properties of water under different temperatures are obtained via the empirical functions (Shinan et al. 2019): $\mu_l = 0.01779/(1 + 0.03368T + 0.000221T^2)$, $\sigma = (75.769 - 0.145T - 0.00024T^2)/1000$. The gas properties are determined according to the reference (Zhu and Zhu, 2016). The detailed physical properties of the liquid and gas phases are shown in Table 4.

According to the numerical results, different outcomes of droplet impact, such as complete rebound, rebound with satellite droplets, and breakup during spreading and splashing, are summarized in Fig. 34 and the four impact outcomes are schematically illustrated in Fig. 35.

Table 4 Physical properties of the water droplet and air phase used in numerical simulations

Temperature (°C)	$\rho_l(kg/m^3)$	$\rho_g(kg/m^3)$	$\mu_l(Pa \cdot s)$	$\mu_g(Pa \cdot s)$	σ(N · m)
−25	999	1.424	6.0×10^{-3}	1.59×10^{-5}	0.0793
−15	999	1.369	3.27×10^{-3}	$1.64 \times 10^{-5}1.64 \times 10^{-5}$	0.0779
0	999.8	1.293	1.78×10^{-3}	1.72×10^{-5}	0.0758
15	999.13	1.226	1.14×10^{-3}	1.79×10^{-5}	0.0736
25	997	1.185	0.898×10^{-3}	1.84×10^{-5}	0.0728

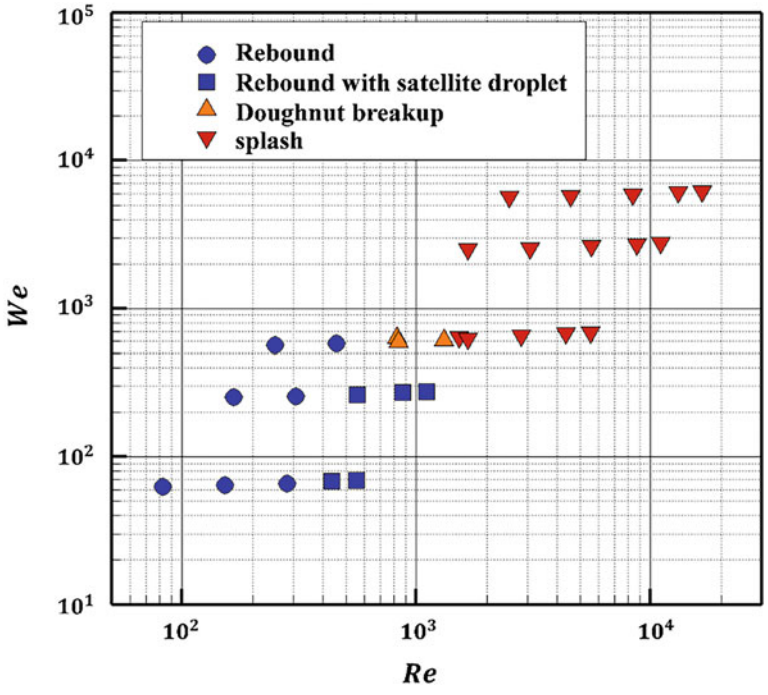

Fig. 34 Droplet impact regimes of numerical simulations

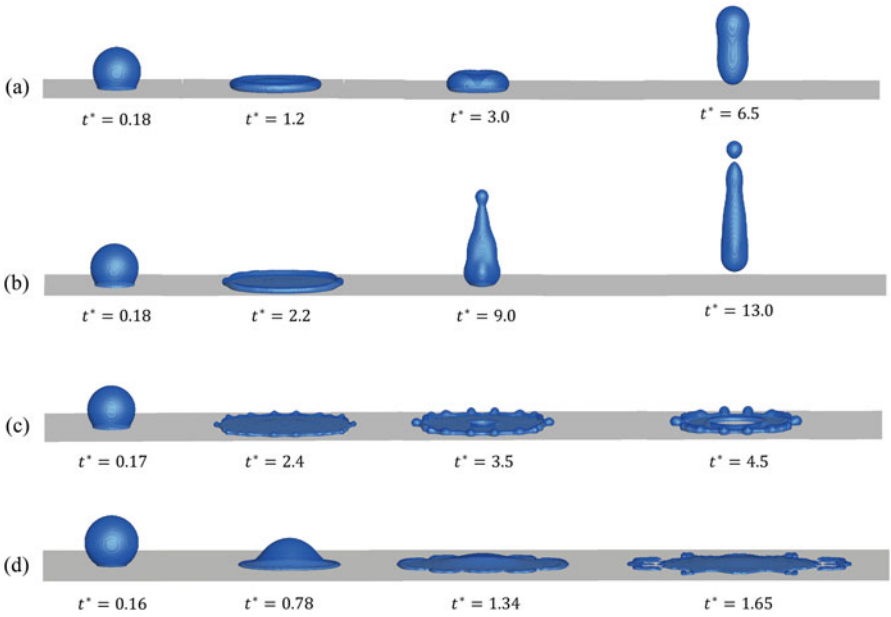

Fig. 35 Schematic of different impact regimes: (**a**) completely rebound, (**b**) rebound with satellite droplet, (**c**) doughnut-breakup, (**d**) splashing

Figures 36 and 37 shows the fingering evolutions for the cases of droplet impact without breakup. The maximum number of fingers generally appears when the droplet reaches its maximum spreading state. Then the fingers start to coalesce, resulting in a decrease in finger numbers. In addition, the finger size and the separation with the lamella increase with *Re*.

An analytical model is proposed by Aziz et al. (Aziz and Chandra 2000) to predict the maximum number of fingers around the periphery of the droplet. The expression of the model is in the formulation of

$$N = \sqrt{\frac{We\sqrt{Re}}{48}} \tag{47}$$

As shown in Fig. 38, the numerical results show a good agreement with the analytical model from Aziz et al. (Aziz and Chandra 2000).

The splashing threshold plays an important role in many industrial applications and is wildly investigated in droplet impingement research. A general expression of the splashing model can be given as

$$We^a\, Re^{\,b} = K \tag{48}$$

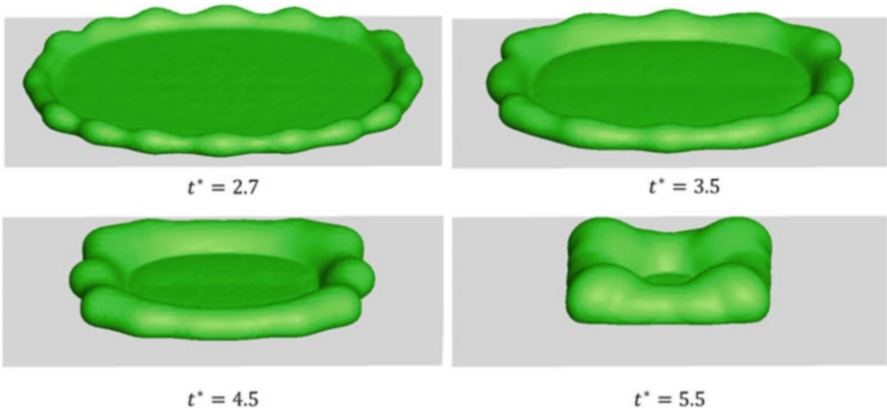

Fig. 36 Snapshot of droplet fingering evolutions with conditions T = 15 °C, D_0 = 50 μm and U_0 = 20 m/s

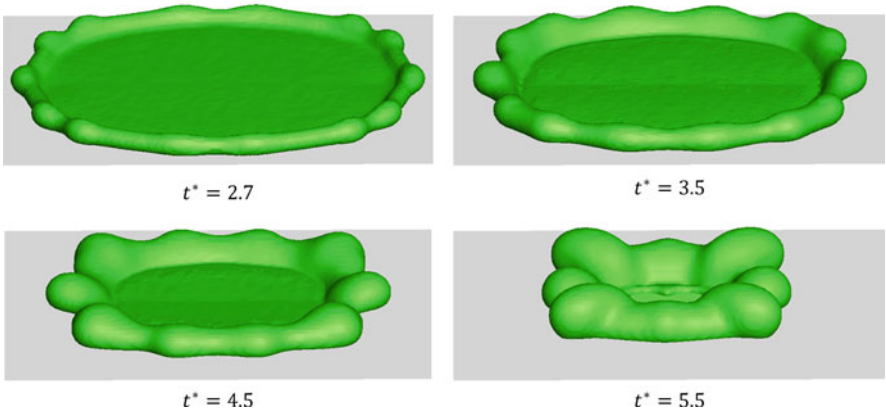

Fig. 37 Snapshot of droplet fingering evolutions with conditions T = 25 °C, D_0 = 50 μm and U_0 = 20 m/s

where K is the droplet splashing threshold. Based on the present numerical and experimental results, the expression of the proposed impact model is given in the form of:

$$We^{0.25}\, Re^{0.25} = 25.15 \tag{49}$$

As shown in Fig. 39, the splash criterion of We decreases under a high Re region. It is because as Re increases, the inertial force of the droplet becomes dominant, the periphery of the droplet cannot be maintained by surface tension force, and breakup occurs.

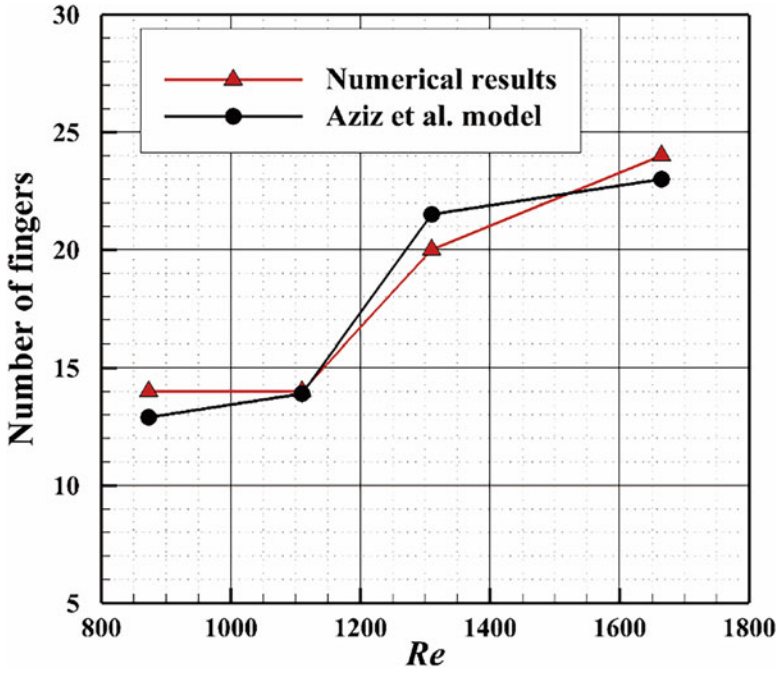

Fig. 38 Comparison of the maximum number of fingers between numerical results and analytical model.

Droplet Impact on Superhydrophobic Surfaces with Protrusions

Except for those above, the droplet impact on the superhydrophobic surfaces with protrusions is numerically investigated. In which, a three-dimension pseudopotential LBM is employed due to its advantage in dealing with the curved boundary. It should be noted that all the parameters in this section are all based on lattice units, which is typical in Lattice Boltzmann simulations. Figure 40a illustrates the schematic of a droplet impacting a superhydrophobic surface with protrusions and protrusion shapes. In the simulations, a droplet with a diameter of 80 lu is initially located at several lu above the protrusion whose characteristic length is W lu without gravity to obtain an equilibrium state. After 10,000 time steps, the droplet (which has reached an equilibrium state) is released with a falling velocity, u_0. The different shapes of protrusions consisting of triangle protrusion, square protrusion, and circle protrusion are considered in this study, as shown in Fig. 40b. In the present work, to reduce and facilitate the research, only the cases in which the height of the isosceles triangle and square are the same as W is considered here. The 3D computational domain with dimensions of $341 \times 241 \times 151$ lu^3 is applied with periodical boundary conditions on all sides of the domain and non-slip boundary conditions on the top and bottom. In addition, the specific curved boundary treatment that can effectively overcome the mass leakage problem described in the previous section is applied here.

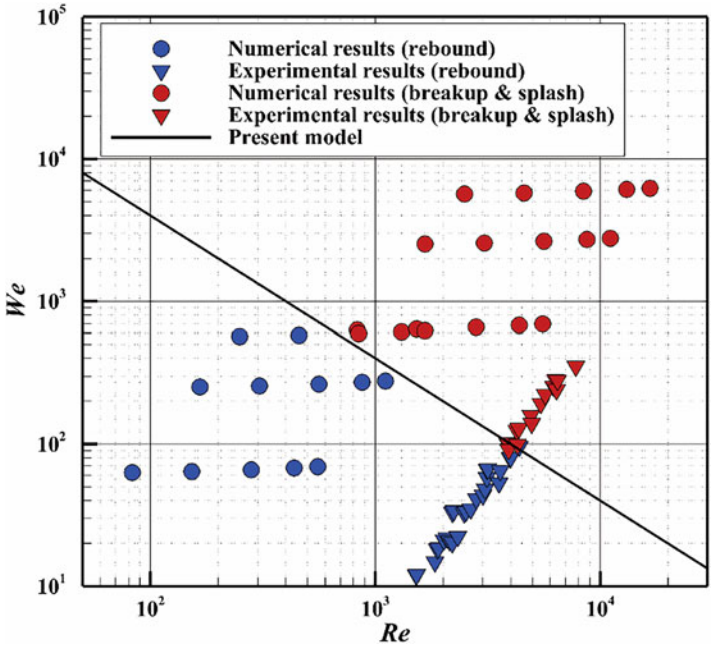

Fig. 39 Droplet impact regimes and proposed impact splashing criteria

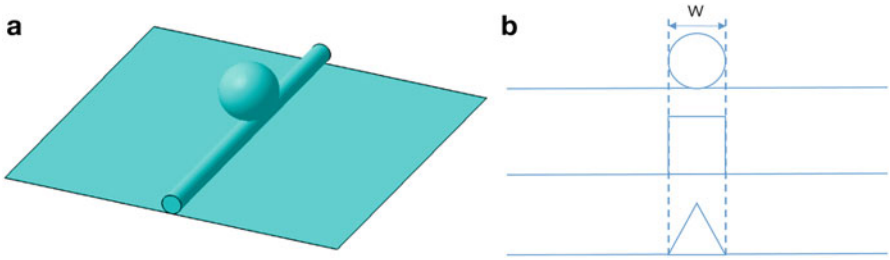

Fig. 40 Schematic of (**a**) a droplet impacting a superhydrophobic surface decorated with a protrusion and (**b**) protrusion shapes

In general, the droplet impact process can be divided into three stages: (a) the falling stage, (b) the spreading and retraction stage, and (c) the lifting-up stage. The $t = 0$ is taken as the moment when the droplet just contacts with the top of the protrusion, and the durations for the three stages can be noted as t_1, t_2, and t_3. Thus, the whole contact time can be defined as $t_c = t_1 + t_2 + t_3$. Unless otherwise specified, the time t used in this section is nondimensionalized by $\sqrt{\rho R^3/\sigma}$.

Figure 41a shows the dimensionless time t^* which is defined as $t^* = t/t_{cflat}$ for different *We*. It can be seen that when $We \leq 5.2$, the contact time is more than that on the flat surface. This negative effect is attributed to the fact that more time is required

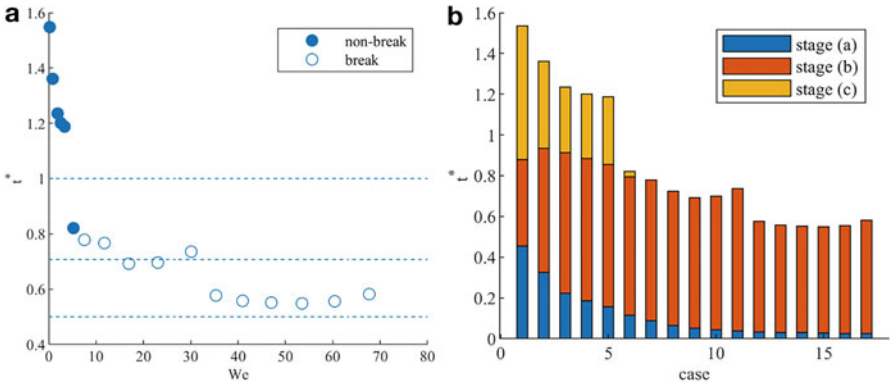

Fig. 41 (**a**) Contact time as a function of *We* for $W = 16$, (**b**) The proportion of three stages to the total time (case 1 to 17 correspond to We from small to large)

for the droplet to move down and up the protrusion and the spreading speed on the bottom wall is also significantly reduced. This phenomenon was also reported in previous experimental studies (Jiang et al. 2020; Hu et al. 2021). When $5.2 < We < 35.3$, as shown in Fig. 41b, the proportion of stage (a) and stage (c) decreases significantly with increased *We*. Even when *We* is greater than 7.5, stage (c) no longer exists, and the contact time of droplets will be effectively reduced due to the occurrence of the break-up. With the further increase of *We*, the time for stage (b) will dramatically decrease. As shown in Fig. 41a, a step-like shape of reduced contact time occurs at $We = 35.3$ caused by the transition from twice-retraction to once-retraction and the contact time exhibits two reduced values, which are 0.75 and 0.56 at moderate and high *We* respectively. Those phenomena are consistent with previous experiments (Gauthier et al. 2015).

The instantaneous droplet velocity v_z is introduced to quantitatively describe the movement trend of the droplet in the vertical direction, which is defined as a mass-averaged *z*-component velocity

$$v_z = \frac{\int_\Omega \rho_l v_z d\Omega}{\int_\Omega \rho_l d\Omega} \tag{50}$$

where Ω represents the droplet computational domain. The parts are marked by a black circle in Fig. 42 represents the moment when the droplet just touches the bottom wall and the corresponding dimensionless z component velocities $v_z^* = v_z/v_i$ where v_i is the droplet falling velocity are 0.85, 0.96, and 0.97 at $We = 1.88$, 16.93 and 47.01, respectively, which means the loss of kinetic energy in stage (a) becomes smaller with increased *We*. In addition, in Fig. 42, it can be found that v_z is approximately linearly related to t from droplets touching the bottom wall to the moment $v_z = 0$ which means during this process, the acceleration is almost

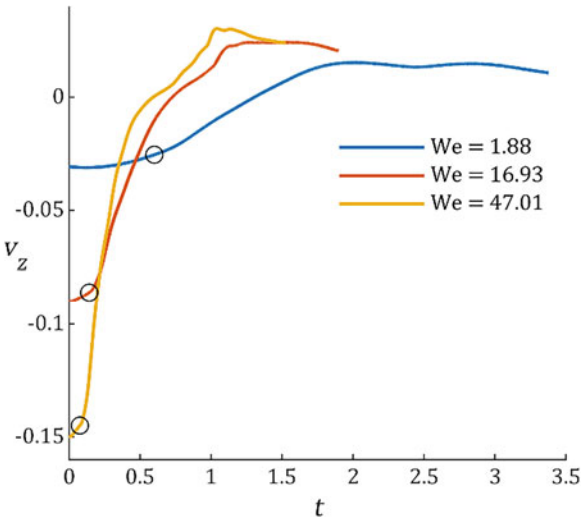

Fig. 42 The evolution curve of v_z at $We = 1.88$, 16.93, and 47.01 (the marked part represents the moment when the droplet just touches the bottom wall)

constant and approximately satisfies the quadratic relationship with *We* which can be written as $k = -0.00006689We^2 + 0.008974We - 0.02469$ where k is the scaling coefficient (acceleration).

As discussed, there are two critical *We* 5.2 and 35.3 to distinguish whether the protrusion can effectively reduce the contact time and the efficiency of reducing the contact time, respectively. Therefore, to facilitate discussion, the low, moderate, and high *We* regimes are defined, respectively, as *We* lower than 5.2, *We* between 5.2 and 35.3, and $We \geq 35.3$.

To investigate the influence of protrusion size on contact time, its shape is kept unchanged while its size *W* is changed in the range of 10–30. As shown in Fig. 43, three different rebound ways can be observed in our simulations, which are noted as non-break bouncing, two droplets bouncing and three droplets bouncing, respectively. Figure 44a shows the specific type of bouncing corresponding to different *We* and *W*, and it can be found that when the size of the protrusion and *We* increase, there will be a transition from non-break bouncing to two droplets bouncing, and then to three droplets bouncing.

The contact time of droplets at different *We* and *W* are shown in Fig. 44b. In the low *We* regime, the droplet needs to spend more time moving down and up along the protrusion with increased *W*. Therefore, the contact time of the droplet will increase with protrusion scale *W*. In the moderate *We* regime, the increase of *W* leads to the deformation of the fragments on both sides of the protrusion to be more drastic, which results in a great reduction in contact time. However, with *W* and *We* are increasing further, the transition of bouncing type from two droplets bouncing to three droplets bouncing occurs, which increases the contact time. Under these comprehensive effects, the whole contact varies slightly with the change of *W* but is affected significantly in the high *We* regime. As shown in Fig. 45, when

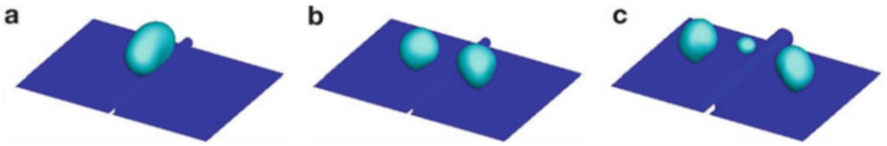

Fig. 43 Different types of bouncing: (**a**) non-break bouncing, (**b**) two droplets bouncing, and (**c**) three droplets bouncing

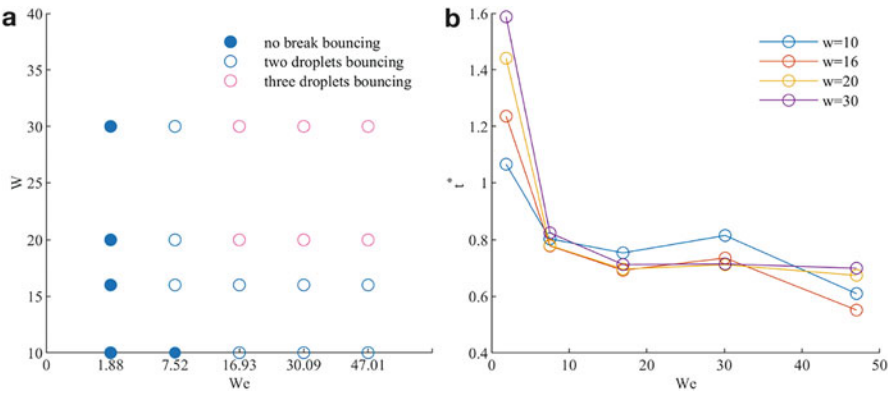

Fig. 44 The effects of W on (**a**) the types of bouncing and (**b**) the contact time for various We

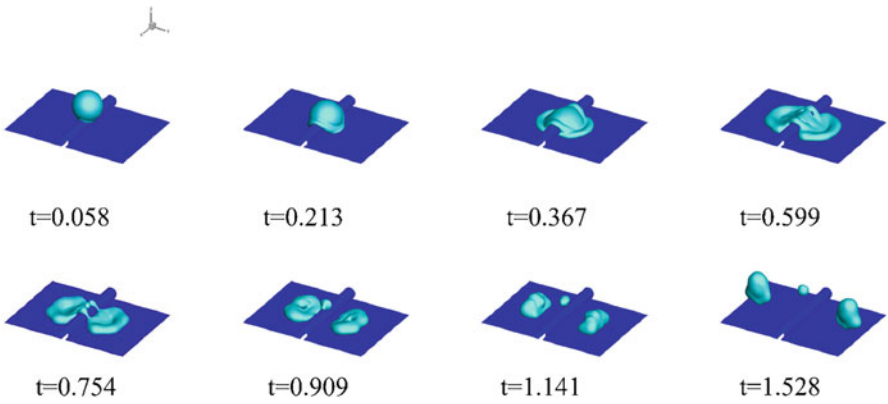

Fig. 45 Snapshots of a droplet impacting a superhydrophobic surface with a cylindrical protrusion of $W = 30\ lu$ at $We = 47.01\ lu$

W increases to $30lu$, the fragments on both sides of the protrusion no longer evolve into four apparent branches. In addition, two obvious cavities can be observed in the center of the liquid films, leading to a larger surface area. In the process of droplet contraction, the surface energy is transformed into kinetic energy and potential

energy. The larger the surface area, the smaller the kinetic energy of the liquid film. In addition, the small droplets formed above the protrusion prematurely take away part of the kinetic energy. The reduction of kinetic energy leads to the rebound speed v_z at $W = 30\ lu$ is lower than that at $W = 16\ lu$, except for the starting point and end point shown in Fig. 46. Therefore, the droplet rebounds earlier at $W = 16\ lu$ than at $W = 30\ lu$.

In addition, the effects of different protrusion shapes on contact time are also examined. In the low and moderate *We* regimes, although the time proportion of the three stages varies, the whole contact is almost the same, as shown in Fig. 47.

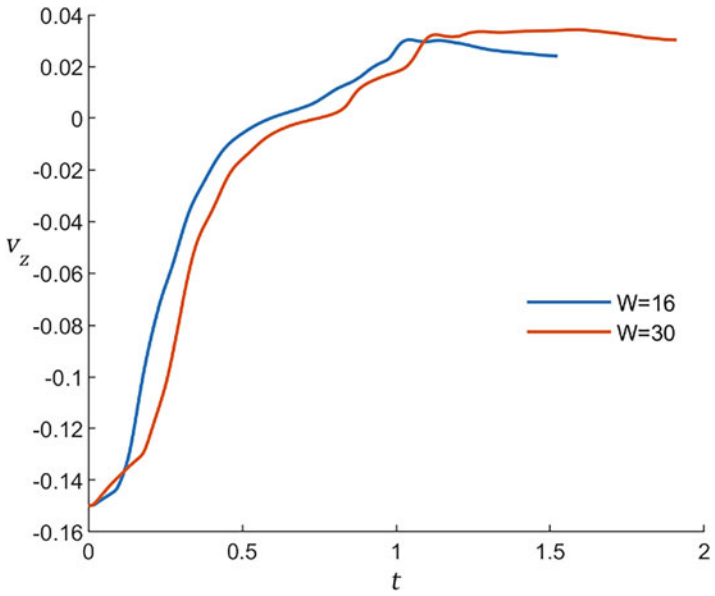

Fig. 46 The evolution curve of v_z for $W = 16\ lu$ and $W = 30\ lu$ at $We = 47.01$

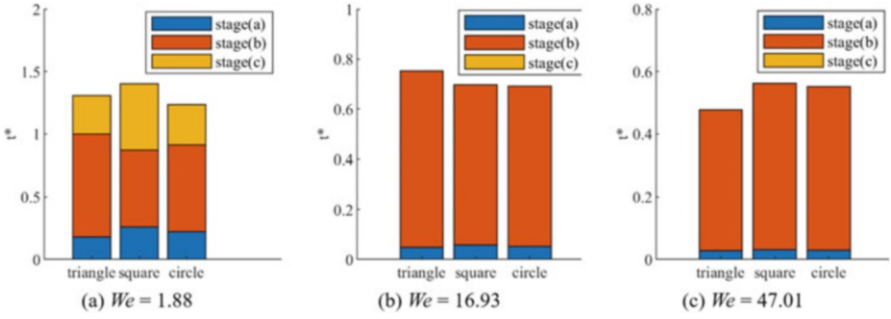

Fig. 47 The contact time and the proportion of different stages for different *We* and protrusions. (**a**) $We = 1.88$. (**b**) $We = 16.93$. (**c**) $We = 47.01$

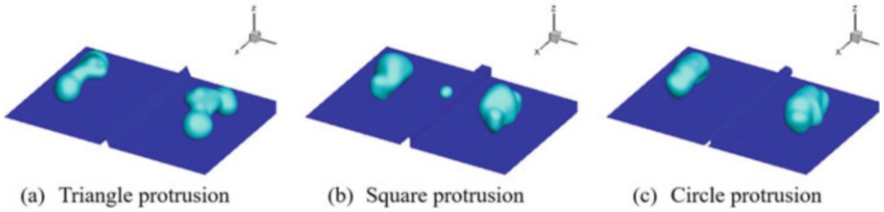

Fig. 48 Schematics of droplets leaving the surface for different protrusions. (**a**) Triangle protrusion. (**b**) Square protrusion. (**c**) Circle protrusion

However, in the high *We* regime, the retraction way, and the types of bouncing which are responsible for the variation of contact time depend on the protrusion shape. Figure 48 shows the droplet dynamics when droplets leave the surface, and it can be found that the completion rate of twice-retraction determines the order of the time for droplets' bounce-off. In addition, because the droplet contacts the square protrusion by a curved surface to a plane surface, different from a curved surface to a line for the circle and triangle protrusion, which makes the droplet spread on the top of the square protrusion and vertical plane successively, it is more easily for a small droplet to be formed on the top of square protrusion as shown in Fig. 48b. This transition from two droplets bouncing to three droplets bouncing increases the contact time. According to the numerical results, in the high *We* regime, the time for droplets bounce-off are in order: square $>$ circle $>$ triangle, and the contact time of the droplet impacting on a superhydrophobic surface decorated with triangle protrusion can effectively be reduced up to 48% compared with a flat surface.

Conclusions

In this section, two topics are numerically investigated: droplet impact on a flat superhydrophobic surface and a superhydrophobic surface with a single protrusion. For the first topic, the level-set method is employed, and the results reveal that: four different impact regimes are observed and studied, which include completely rebound, rebound with satellite droplet, doughnut breakup, and splashing. For the cases of droplet impact without breakup, it can be found that the maximum number of fingers appears when the droplet reaches its ultimate spreading state. Then the fingers begin to coalesce, leading to a decrease in finger numbers. In addition, our numerical results show a good agreement with the analytical model from Aziz et al. (Aziz and Chandra 2000). Due to the importance of the splashing threshold in many industrial applications, based on present numerical and experimental results, a new impact spread/splash model is also proposed, which can be given as: $We^{0.25}Re^{0.25} = 25.15$.

Then, the dynamic behavior of a droplet impacting a superhydrophobic surface with protrusions is numerically studied via the 3D pseudopotential Lattice Boltzmann method, which is in the form of reduced values. For the case of the

superhydrophobic surface with a single protrusion, it is found that the droplet exhibits different non-axisymmetric dynamics for various *We* and *W*, including three bouncing ways (non-break bouncing, two droplets bouncing, and three droplets bouncing) and two retraction ways (once-retraction and twice-retraction). Specifically, in the low *We* regime, the contact time increases with *We* and *W* due to the additional time required for the droplet to move along the protrusion. In the moderate *We* regime, since the droplet is split into two small fragments leading t_3 to be zero, the contact time is effectively reduced. In the high *We* regime, a further decrease in contact time can be observed due to the transition from twice-retraction to once-retraction. On the other hand, the factor *W* has little influence on the contact time for the moderate *We* regime; while in the high *We* regime, the large *W* facilitates the occurrence of three droplets bouncing, which will greatly hinder the reduction in contact time. While in terms of the shape of protrusions, the way droplets contact with the protrusion varies from a curved surface to a plane surface for square protrusions to a curved surface to a line for the circle and triangle protrusion. It is observed that the contact reduction is inefficient for the square protrusion compared with circle and triangle protrusions.

Droplet Freezing

In this section, the droplet freezing process on surfaces with different wettability is simulated through the multiphase lattice Boltzmann flux solver (Wang et al. 2015a, b) and the enthalpy porosity model. The temperature evolution of the droplets is visually illustrated to identify the phenomenon involved in the cooling and phase change of the droplets.

Multiphase Lattice Boltzmann Flux Solver and Phase Field Method

The mass, momentum, and energy equations for incompressible flow with phase change and volume expansion effect are given by:

$$\frac{\partial \rho}{\partial t} + \nabla \cdot \rho \boldsymbol{u} = 0 \tag{51}$$

$$\frac{\partial \rho \boldsymbol{u}}{\partial t} + \nabla \cdot (\rho \boldsymbol{u}\boldsymbol{u}) = -\nabla p + \nabla \cdot \left[\mu\left(\nabla \boldsymbol{u} + (\nabla \boldsymbol{u})^T\right)\right] + \boldsymbol{F}_s \tag{52}$$

$$\frac{\partial \rho^m C_p^m T}{\partial t} + \nabla \cdot \left(\rho^m \boldsymbol{u} C_p^m T\right) = -\rho^m C L \frac{\partial \gamma}{\partial t} + \nabla \cdot (k^m \nabla T) \tag{53}$$

where t is time, p is pressure, ρ is density, $\boldsymbol{u}$ is velocity, c_s is the speed of sound, μ is dynamic viscosity, ρ_l is water density, ρ_s is ice density, L is the latent heat of water, T is temperature, C_p is specific heat capacity, k is thermal conductivity, and $\boldsymbol{F}_s$ is source term, including gravity force and surface tension force. γ in the energy

equation, the liquid fraction takes 0 in the pure ice phase and 1 in the pure non-ice phase, while C is the non-air fraction that takes 0 in the pure air phase and 1 in the pure non-air phase. The material properties with superscript m refer to the mean value of the pure material properties, which take the following form:

$$\psi^m = \psi_a + C[\psi_s + \gamma(\psi_l - \psi_s) - \psi_a] \tag{54}$$

where ψ represents either ρ, C_p, or k while ψ with subscripts a, l, or s are properties of air, water, or ice, respectively. Moreover, it is noted that the above equations are not closed due to the independence of the liquid fraction. A supplementary equation is required to correlate γ and T. It's assumed that the freezing phenomenon occurs within a narrow temperature band, T_s to T_l, rather than at a certain temperature point. Thus, one optional solution to close flow and energy equations is using a piecewise linear function (Shen et al. 2019; Shinan et al. 2019; Zhang et al. 2020b):

$$\gamma = \begin{cases} 1 & T \geq T_l \\ \dfrac{T - T_s}{T_l - T_s} & T_s < T < T_l \\ 0 & T \leq T_s \end{cases} \tag{55}$$

Actually, the static droplet freezing on the surface could be divided into four distinct stages (Zhang et al. 2018): the droplet first cooled down by the cold surface and this stage is liquid cooling (supercooling). Then, the droplet enters the nucleation stage instantly and completes the recalescence spontaneously, the period of which is so short that compared to the following freezing stage, the nucleation and recalescence stage takes place within several orders of magnitude lower than the duration of the freezing stage. When the droplet is completely frozen, the ice is cooled by the cold surface and this stage is solid cooling. It's worth noted that, after nucleation and recalescence stage, the temperature of the supercooled droplet increases to the freezing point 0 °C due to the release of the latent heat and the droplet is assumed to be uniform. Therefore, the corresponding initial liquid fraction γ_0 is:

$$\gamma_0 = 1 - \frac{C_{pl}\Delta T}{L} \tag{56}$$

where ΔT is the droplet supercooling. The freezing temperature 0 °C and the corresponding liquid fraction serve as the initial conditions in the following simulations.

In addition to the flow and heat transfer governing equations shown above, the following interface-capturing equation is proposed to track the interface between water and air:

$$\frac{\partial C}{\partial t} + \nabla \cdot (C\boldsymbol{u}) = C\left(1 - \frac{\rho_l}{\rho_s}\right)\frac{\partial \gamma}{\partial t} \tag{57}$$

Obviously, from the numerical viewpoint, the right-hand side of the equation accounts for the volume expansion effect, which appears at the liquid water and ice interface. Specifically, $C(1\text{-}\gamma)$, $C\gamma$, and $1\text{-}C$ are referred to as ice, liquid water, and air, respectively.

It should be noticed that instead of adding a damping source term to the momentum equation or specifying the ice viscosity (Karlsson et al. 2018; Attarzadeh and Dolatabadi 2019; Zhang et al. 2020b), which requires the determination of the uncertain coefficient, the following treatment is implemented to ensure the stagnant state inside the frozen ice area:

$$\boldsymbol{u} = \boldsymbol{u}[C(\gamma - 1) + 1] \tag{58}$$

For the flow field solution, the improved multiphase Lattice Boltzmann flux solver (Wang et al. 2015a, b) in a cylindrical coordinates system is applied, while the energy equation is solved by a finite difference method using a second-order upwind scheme. In addition, the finite volume method is utilized to solve the interface capturing equation where the fifth-order WENO scheme is adopted to increase accuracy.

Validation of the Method

The droplet freezing on the cold surface is simulated by applying the above-introduced multiphase Lattice Boltzmann flux solver and phase field method. The initial conditions are as follows: equivalent diameter of the droplet D is 2.93 mm, relative humidity is $36.7 \pm 1\%$, surface temperature T_{wall} is -10.7 ± 0.1 °C while air temperature T_{air} is -5.7 ± 0.1 °C, and contact angle of the test plate CA is 120°. The numerical result is compared with the experimental data in Fig. 49, where the representative four frames are presented.

It is indicated that the ice develops from the plate surface to the top of the droplet and the water-ice interface evolves from flat to concave. Finally, the entire droplet presents a peach-like shape due to the volume expansion of the freezing

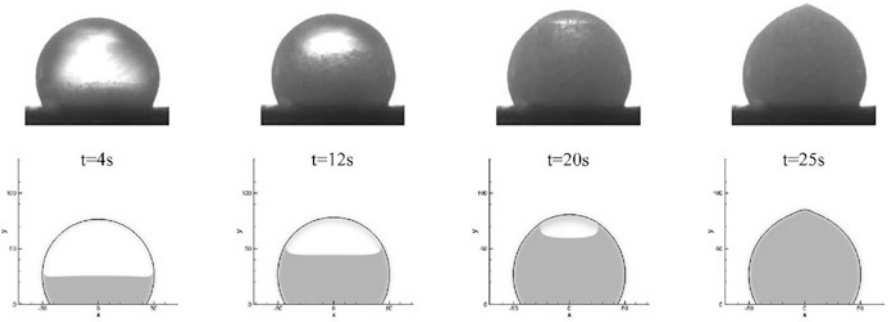

Fig. 49 Comparison of the droplet freezing process between the experiment and simulation

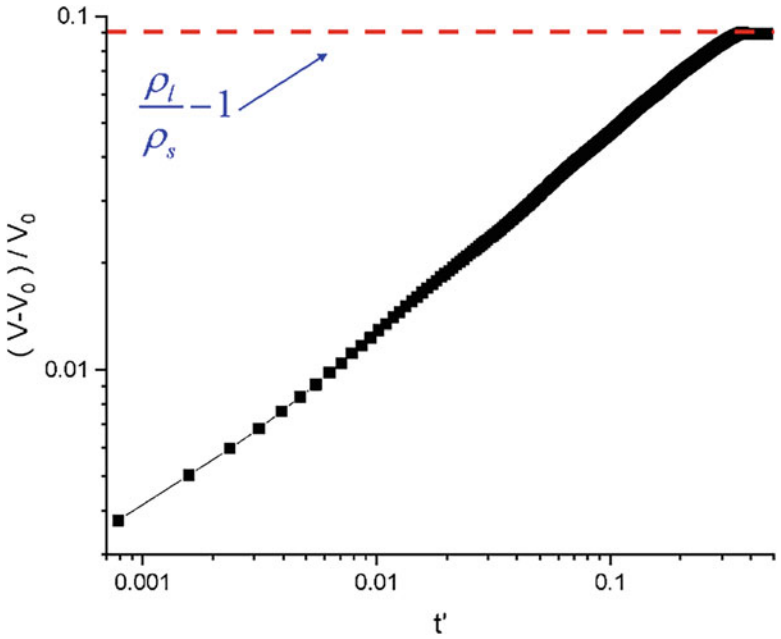

Fig. 50 The computational result of expansion degree

process. Two non-dimensional variables are defined here: the expansion degree of droplet volume evaluated by the relative volume expansion ratio $(V\text{-}V_0)/V_0$, where V is the droplet volume while V_0 is its initial volume, and dimensionless time $t' = tk_l/(\rho_l C_{pl} D^2)$. The computational result of the expansion degree is shown in Fig. 50. The droplet expansion degree increases with time and finally coincides with the theoretical value $\rho_l/\rho_s - 1$, which verifies the droplet mass conservation in the simulation. The qualitative and quantitative comparisons confirmed that the introduced numerical method could accurately capture the droplet freezing process on a cold surface.

Results and Discussions

The dynamic droplet freezing process on the cold plate is governed by several factors, including droplet equivalent diameter D, the contact angle of the plate surface CA, supercooling of the droplet ΔT, and cooling of the plate T_{wall}. In this part, T_{air} and ΔT are equal to T_{wall}, and the effects of D, CA, and T_{wall} are analyzed. The normalized temperature θ is hereby introduced and defined as $\theta = -T/T_{wall}$.

Effect of Droplet Size

The droplet sizes suspended in the air encountered by the aircraft are usually from tens of micrometers to hundreds of micrometers. The droplets with diameters of

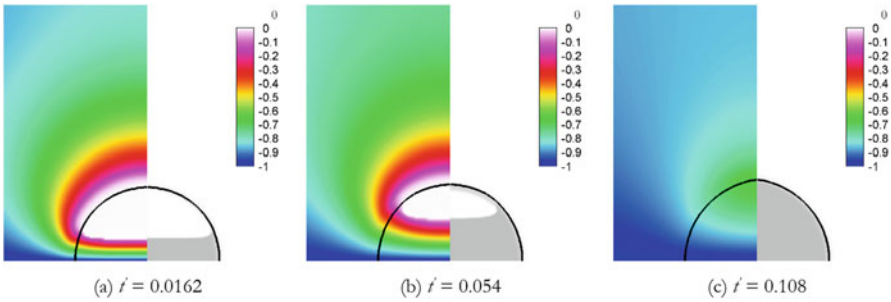

Fig. 51 The freezing process of 500 μm diameter droplet on the −20 °C surface with a contact angle of 90°. (**a**) $t' = 0.0162$. (**b**) $t' = 0.054$. (**c**) $t' = 0.108$

50 μm, 500 μm and 2 mm on the −20 °C surface with a contact angle of 90° are simulated. As the ice-water and liquid-gas interface development processes are similar for different-sized droplets, Fig. 51 only shows the ice formation and growth, as well as the temperature evolution of 500 μm diameter droplet.

It is evident from Fig. 51 that the ice accumulates from the bottom initially with nearly the flat shape, and the expanded volume pushes the liquid water upwards. With the development of the freezing, the water-ice interface presents the concave profile, as shown in Fig. 51b, implying that the ice freezes more rapidly at the droplet surface than at the center. Furthermore, the liquid water surface is frozen, but the motion is not significantly affected, which is inconsistent with the experiments (Marin et al. 2014; Zhang et al. 2018). However, because of continuous cooling from the plate surface, the entire droplet finally turns into ice, and a bulge is formed on the top, as described in Fig. 51c. And the latent heat is released, as seen from the temperature distribution.

It's shown in Fig. 52 that the temperature distributes along the droplet's symmetrical axis at different times, where the horizontal axis represents dimensionless height z/D. The temperature within the droplet declines continuously while that of the air increases firstly and then decreases to the temperature of the plate surface. With the global evolution of the temperature field presented in Fig. 52, it is inferred that the air is heated by the convection and conduction between the droplet and air. However, the plate surface cools down the air, and the cold air gradually develops to surround the unfrozen water. As heating from the droplet to the air is weaker than cooling the cold upper air, the temperature of the air above the droplet decreases when $t^* = 0.108$.

Effect of Droplet Supercooling

The droplet freezing processes under different plate cooling temperatures are simulated and the effect of the cooling temperature ranging from −10 °C to −20 °C is discussed. The evolutions of the water-ice interface and temperature distribution where three moments of each case are selected as approximately 15%, 50%, and 100% of the droplet total freezing time are shown in Figs. 53 and 54.

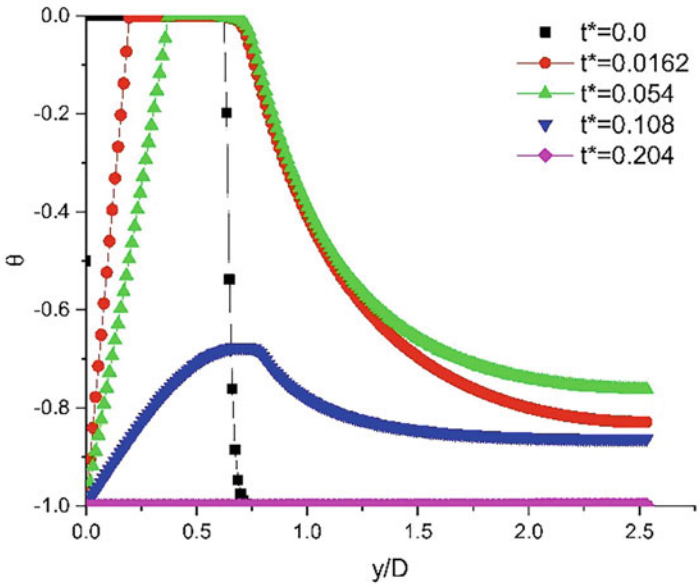

Fig. 52 Temperature distributions on the droplet symmetrical axis

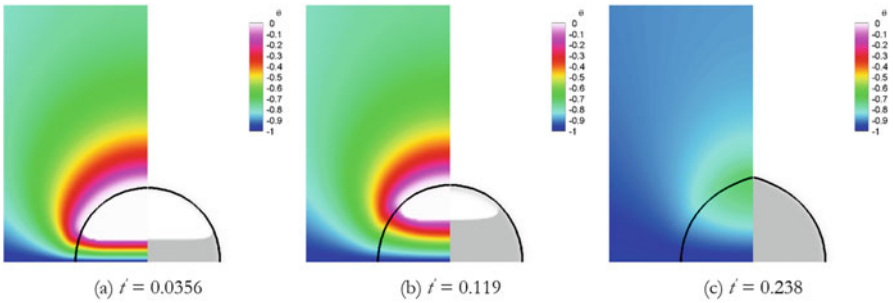

Fig. 53 The freezing process of 500 μm diameter droplet on the −10 °C surface with a contact angle of 90°. (**a**) $t' = 0.0356$. (**b**) $t' = 0.119$. (**c**) $t' = 0.238$

Despite the droplets experiencing a similar ice growth process under different plate cooling temperatures, its effect is distinct from that of the droplet size. They spend unequal time under dimensionless units. The lower the plate cooling temperature, the shorter it takes for the droplet to be frozen completely. The total freezing time increases to around 2.2 times when the plate temperature varies from −20 to −10 °C. It is also found that the heating from droplets' latent heat release on the air is weaker than that under higher plate cooling temperatures at 15% of droplets' total freezing time. This is mainly because of the lower initial air temperature and the larger supercooling of the droplet, with which the droplet has consumed more latent heat to rise to the freezing point at the recalescence stage.

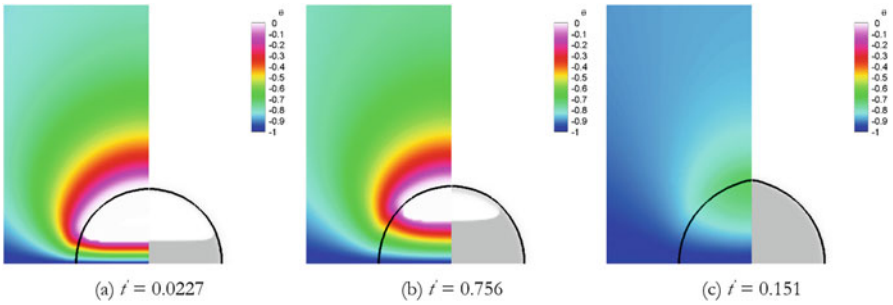

Fig. 54 The freezing process of 500 μm diameter droplet on the −15 °C surface with a contact angle of 90°. (**a**) $t' = 0.0227$. (**b**) $t' = 0.756$. (**c**) $t' = 0.151$

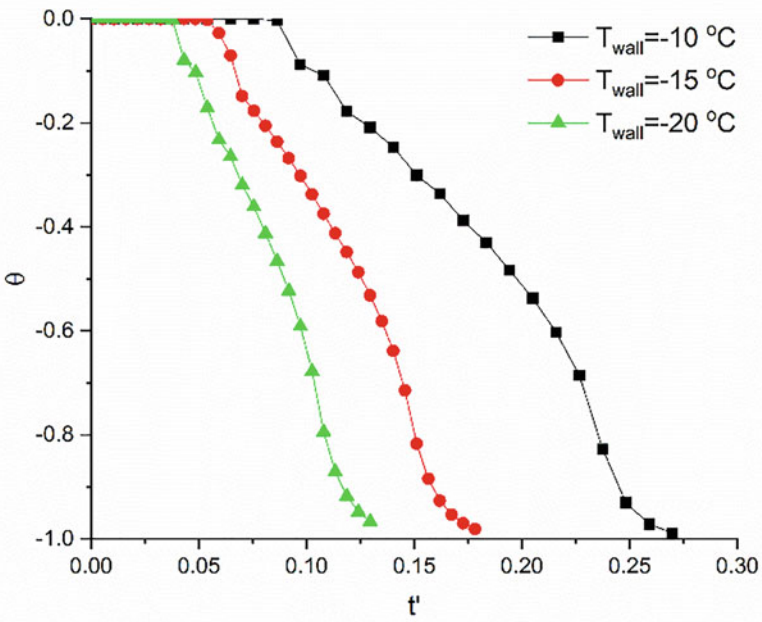

Fig. 55 Temperature variations at 50% height of the initial droplet centerline

The temperature variations versus time at 50% height of the initial droplet centerline for the droplet on a cold plate with different cooling temperatures are described in Fig. 55. The droplet duration at a freezing point is prolonged by the smaller droplet supercooling and higher plate temperature, which raises every 5 °C, greatly increasing the time to reach the identical dimensionless temperature.

Effect of Surface Wettability

The droplets freezing on the plates with different surface wettability could present different frozen shapes, and the temperature distributions during the freezing process

are correspondingly changed. The simulation results for droplets freezing on the plates with contact angles of 60° and 150° are presented in Figs. 56 and 57.

It is obvious that when the plate surfaces are hydrophilic and neutral (contact angle varies from 60° to 90°), the profiles of the ice fronts show flat first and gradually transit to concave. While for the superhydrophobic plate surface in Fig. 57, the ice front is convex before the flat shape appears, indicating the larger ice growth velocity in the center. Correspondingly, the temperature distribution inside the droplet near the plate surface is not approximately zero gradients along the radial direction. The reason for the convex ice front is that when the bottom ice layer forms, the heat transfer is stronger between the ice in the center and the above liquid water, while that is weaker at the droplet's lateral root, where the liquid water contacts with the lower conductivity air compared to the ice. Another important characteristic is that the temperature inside the droplet could stay higher when the droplet is frozen instantaneously compared to the droplet on the hydrophilic surface. This is related to the limited heat transfer area so that the ice accumulation velocity is slower, and the cooling effect of the plate is weaker in the upper part of the droplet.

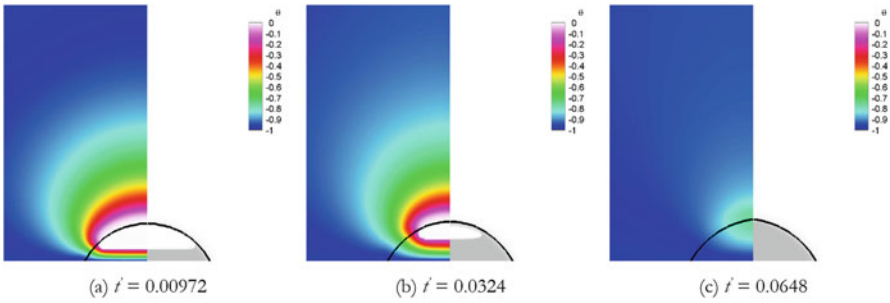

Fig. 56 The freezing process of 500 μm diameter droplet on the −20 °C surface with a contact angle of 60°. (**a**) $t' = 0.00972$. (**b**) $t' = 0.0324$. (**c**) $t' = 0.0648$

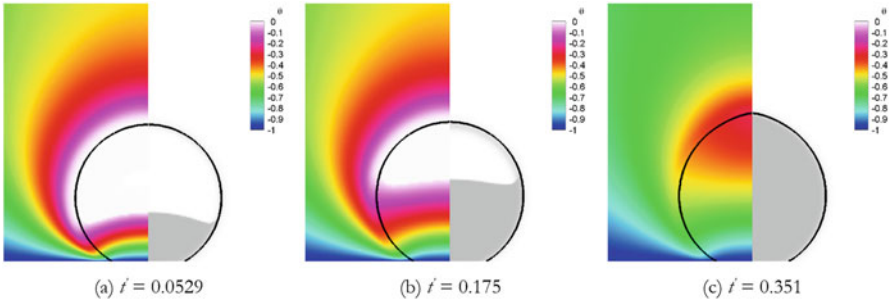

Fig. 57 The freezing process of 500 μm diameter droplet on the −20 °C surface with a contact angle of 150°. (**a**) $t' = 0.0529$. (**b**) $t' = 0.175$. (**c**) $t' = 0.351$

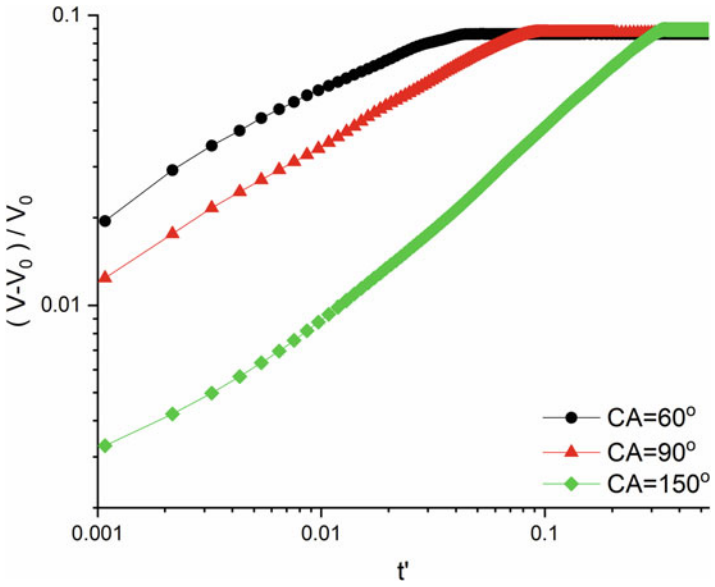

Fig. 58 Temperature distributions on the droplet centerline

Hence, with the release of droplets' latent heat, the cooling effect from the plate on the surrounding air is relatively decreased.

The droplet volume expansion degrees for droplet freezing on surfaces with different wettability are depicted in Fig. 58. For the neutral surface, the expansion degree increases linearly with time in double logarithm coordinates while the growth curves slightly deviate from the linear relation for $CA = 60°$ and 150° but finally reach the identical relative volume expansion ratio. It is also illustrated that the total freezing time increases to around 5.4 times when the contact angle varies from 60° to150°, which is also suggested in Fig. 57.

Conclusions

In this section, the droplet freezing process on the cold surface is investigated through the developed multiphase Lattice Boltzmann flux solver and phase field method. Three main impact factors, droplet equivalent diameter D (ranging from 50 μm to 2 mm), plate surface temperature T_{wall} (ranging from −10 to −20 °C), and plate surface contact angle CA (ranging from 60 to 150°), are considered seriously in the fully unsteady droplet phase change process. The developed solver is confirmed to be accurate by comparing the experimental and theoretical results.

The numerical results show that the droplet size leads little effect on the freezing process of the droplet. In contrast, the cold plate temperature and surface wettability significantly impact more. When the temperature of the cold plate increases from −20 to −10 °C, the total freezing time increases to around 2.2 times due to the less

latent heat released during the recalescence stage. Besides, the droplet freezing on the superhydrophobic surface shows a convex ice front before a flat water-ice interface followed by a concave shape. And the total freezing time increases to around 5.4 times when the contact angle varies from 60° to 150°.

Conclusions

The supercooled water droplet contained in clouds are the main cause of aircraft icing. During aircraft aviation, the supercooled water droplets ahead the aircraft will go through deformation, impact with aircraft and finally freezing on the aircraft surface. A better understanding of the mechanisms of the movement and thermodynamics of supercooled water droplet is critical for aircraft icing protection systems. When droplet is surrounded by air and the relative velocity between droplet and air is presented, the droplet deformation occurs due to interface instability. The present numerical results indicate that the droplet is in vibration mode, and it can retain the initial spherical shape when $We < 1$. For higher Weber number with range $We < 10$, the droplet is in a transition mode, where periodical deformations are observed. As We is greater than the critical value 10, the droplet is in bag breakup mode. Additionally, with the same initial droplet diameter D_0 and uniform airflow velocity U_g, the extent of deformation is decreased for supercooled water droplets compared to the results with room temperature.

For droplet impingement onto a solid surface, the numerical research reveals four different impact regimes: completely rebound, rebound with satellite droplet, doughnut breakup, and splashing. For the cases of droplet impact without breakup, it can be found that the maximum number of fingers appears when the droplet reaches its ultimate spreading state. Then the fingers begin to coalesce, leading to a decrease in finger numbers. Since the splashing threshold is a critical parameter in many industrial applications, a new impact spread/splash model for superhydrophobic surface is proposed based on present numerical and experimental results: $We^{0.25}Re^{0.25} = 25.15$. Numerical research is also conducted for the droplet impacting onto a superhydrophobic surface with protrusions. It is found that with protrusions existing, the droplet exhibits different non-axisymmetric dynamics for various We and the protrusion characteristic length W. The main dynamics include three bouncing ways (non-break bouncing, two droplets bouncing, and three droplets bouncing) and two retraction ways (once-retraction and twice-retraction). When weber number is low, the contact time increases with We and W due to the additional time required for the droplet to move along the protrusion. In the moderate We regime, the contact time is effectively reduced. In the high We regime, a further decrease in contact time can be observed due to the transition from twice-retraction to once-retraction. While in terms of the shape of protrusions, the way droplets contact with the protrusion varies from a curved surface to a plane surface for square protrusions to a curved surface to a line for the circle and triangle protrusion. It is observed that the contact reduction is inefficient for the square protrusion compared with circle and triangle protrusions.

Since the existing temperature difference between droplet and surface, the supercooled droplet will go through freezing once it is attached to cooling surface. The present numerical results indicate that the droplet size leads little effect on the freezing process of the droplet. In contrast, the cold plate temperature and surface wettability significantly impact more. When the temperature of the cold plate increases from −20 to −10 °C, the total freezing time increases to around 2.2 times due to the less latent heat released during the recalescence stage. Besides, the droplet freezing on the superhydrophobic surface shows a convex ice front before a flat water-ice interface followed by a concave shape. And the total freezing time increases to around 5.4 times when the contact angle varies from 60° to 150°.

References

Abolghasemibizaki M, Mohammadi R (2018) Droplet impact on superhydrophobic surfaces fully decorated with cylindrical macrotextures. J Colloid Interface Sci 509:422–431

Andrew M, Liu Y, Yeomans JM (2017) Variation of the contact time of droplets bouncing on cylindrical ridges with ridge size. Langmuir 33:7583–7587

Attarzadeh R, Dolatabadi A (2019) Icephobic performance of superhydrophobic coatings: a numerical analysis. Int J Heat Mass Transf 136:1327–1337

Aziz SD, Chandra S (2000) Impact, recoil and splashing of molten metal droplets. Int J Heat Mass Transf 43:2841–2857

Bai C, Rusche H, Gosman AD (2002) Modeling of gasoline spray impingement. Atomization spray 12:1–28

Bird JC, Dhiman R, Kwon HM, Varanasi KK (2013) Reducing the contact time of a bouncing drop. Nature 503:385–388

Blake J, Thompson D, Raps D, Strobl T (2015) Simulating the freezing of supercooled water droplets impacting a cooled substrate. AIAA J 53:1725–1739

Brackbill JU, Kothe DB, Zemach C (1992) A continuum method for modeling surface tension. J Comput Phys 100:335–354

Cao Y, Xin M (2020) Numerical simulation of supercooled large droplet icing phenomenon: a review. Arch Comput Methods Eng 27:1231–1265

Cao X-K, Sun Z-G, Li W-F, Liu H-F, Yu Z-H (2007) A new breakup regime of liquid drops identified in a continuous and uniform air jet flow. Phys Fluids 19:057103

Chen L, Xiao Z, Chan PCH, Lee Y-K, Li Z (2011) A comparative study of droplet impact dynamics on a dual-scaled superhydrophobic surface and lotus leaf. Appl Surf Sci 257:8857–8863

Chou WH, Faeth GM (1998) Temporal properties of secondary drop breakup in the bag breakup regime. Int J Multiphase Flow 24:889–912

Coppola G, Rocco G, De Luca L (2011) Insights on the impact of a plane drop on a thin liquid film. Phys Fluids 23:022105

Dai Z, Faeth GM (2001) Temporal properties of secondary drop breakup in the multimode breakup regime. Int J Multiphase Flow 27:217–236

Fedkiw RP, Aslam T, Merriman B, Osher S (1999) A non-oscillatory eulerian approach to interfaces in multimaterial flows (the ghost fluid method). J Comput Phys 152:457–492

Gauthier A, Symon S, Clanet C, Quere D (2015) Water impacting on superhydrophobic macrotextures. Nat Commun 6:8001

Han J, Tryggvason G (1999) Secondary breakup of axisymmetric liquid drops. I. Acceleration by a constant body force. Phys Fluids 11:3650–3667

Hsiang LP, Faeth GM (1995) Drop deformation and breakup due to shock wave and steady disturbances. Int J Multiphase Flow 21:545–560

Hu Z, Wu X, Chu F, Zhang X, Yuan Z (2021) Off-centered droplet impact on single-ridge superhydrophobic surfaces. Exp Thermal Fluid Sci 120:110245
Huang L, Liu Z, Liu Y, Gou Y, Wang L (2012) Effect of contact angle on water droplet freezing process on a cold flat surface. Exp Thermal Fluid Sci 40:74–80
Huang X, Wan K-T, Taslim ME (2018) Axisymmetric rim instability of water droplet impact on a super-hydrophobic surface. Phys Fluids 30:094101
Jain M, Prakash RS, Tomar G, Ravikrishna RV (2015) Secondary breakup of a drop at moderate Weber numbers. Proc R Soc A: Math Phys Eng Sci 471:20140930
Jalaal M, Mehravaran K (2014) Transient growth of droplet instabilities in a stream. Phys Fluids 26:012101
Jiang X, Xu E, Wu G, Li HZ (2020) Drop impact on superhydrophobic surface with protrusions. Chem Eng Sci 212:115351
Jing L, Xu X (2010) Direct numerical simulation of secondary breakup of liquid drops. Chin J Aeronaut 23:153–161
Josserand C, Zaleski S (2003) Droplet splashing on a thin liquid film. Phys Fluids 15:1650–1657
Jung S, Tiwari MK, Doan NV, Poulikakos D (2012) Mechanism of supercooled droplet freezing on surfaces. Nat Commun 3:615
Kang M, Fedkiw RP, Liu X-D (2000) A boundary condition capturing method for multiphase incompressible flow. J Sci Comput 15:323–360
Karlsson L, Ljung A-L, Lundström TS (2018) Modelling the dynamics of the flow within freezing water droplets. Heat Mass Transf 54:3761–3769
Kékesi T, Amberg G, Prahl Wittberg L (2014) Drop deformation and breakup. Int J Multiphase Flow 66:1–10
Krzeczkowski SA (1980) Measurement of liquid droplet disintegration mechanisms. Int J Multiphase Flow 6:227–239
Kulkarni V, Sojka PE (2014) Bag breakup of low viscosity drops in the presence of a continuous air jet. Phys Fluids 26:072103
Kupershtokh AL, Medvedev DA, Karpov DI (2009) On equations of state in a lattice Boltzmann method. Comput Math Appl 58:965–974
Lee W, Son G (2011) Numerical study of droplet impact and coalescence in a microline patterning process. Comput Fluids 42:26–36
Li H, Zhang K (2019) Dynamic behavior of water droplets impacting on the superhydrophobic surface: both experimental study and molecular dynamics simulation study. Appl Surf Sci 498:143793
Li Q, Luo KH, Kang QJ, Chen Q (2014) Contact angles in the pseudopotential lattice Boltzmann modeling of wetting. Phys Rev E 90:053301
Li W, Miao B, Zhu C-L, Zhao N (2020) An experimental study of water droplets deformation and collision with airfoil. Int J Modern Phys B 34:2040094
Li W, Wang J, Zhu C, Tian L, Zhao N (2022) Deformation and acceleration of water droplet in continuous airflow. Phys Fluids 34:033313
Lin D-J, Wang L, Wang X-D, Yan W-M (2019) Reduction in the contact time of impacting droplets by decorating a rectangular ridge on superhydrophobic surfaces. Int J Heat Mass Transf 132: 1105–1115
Ling F, Zhang C, Chen Y (2020) A unified boundary condition based on the halfwat bounce-back scheme in lattice Boltzmann method. J Guangxi Norm Univ, Nat Sci Ed 70
Marin AG, Enriquez OR, Brunet P, Colinet P, Snoeijer JH (2014) Universality of tip singularity formation in freezing water drops. Phys Rev Lett 113:054301
Martin JC, Moyce Penney WJ (1952). An experimental study of the collapse of liquid column on a rigid horizontal plane. Philos Trans R Soc Lond 244:312–324
Mundo C, Sommerfeld M, Tropea C (1995) Droplet-wall collisions: experimental studies of the deformation and breakup process. Int J Multiphase Flow 21:151–173
Nangia N, Griffith BE, Patankar NA, Bhalla APS (2019) A robust incompressible Navier-Stokes solver for high density ratio multiphase flows. J Comput Phys 390:548–594

Obenauf DG, Sojka PE (2021) Theoretical deformation modeling and drop size prediction in the multimode breakup regime. Phys Fluids 33:092113
Patel JK, Natarajan G (2017) A novel consistent and well-balanced algorithm for simulations of multiphase flows on unstructured grids. J Comput Phys 350:207–236
Pilch M, Erdman CA (1987) Use of breakup time data and velocity history data to predict the maximum size of stable fragments for acceleration-induced breakup of a liquid drop. Int J Multiphase Flow 13:741–757
Quan S, Schmidt DP (2006) Direct numerical study of a liquid droplet impulsively accelerated by gaseous flow. Phys Fluids 18:102103
Rakotondrandisa A, Danaila I, Danaila L (2019) Numerical modelling of a melting-solidification cycle of a phase-change material with complete or partial melting. Int J Heat Fluid Flow 76: 57–71
Sanjeevi SKP, Zarghami A, Padding JT (2018) Choice of no-slip curved boundary condition for lattice boltzmann simulations of high-Reynolds-number flows. Phys Rev E 97:043305
Shen M, Li BQ, Yang Q, Bai Y, Wang Y, Zhu S, Zhao B, Li T, Hu Y (2019) A modified phase-field three-dimensional model for droplet impact with solidification. Int J Multiphase Flow 116: 51–66
Shinan C, Liang D, Mengjie S, Mengyao L (2019) Numerical investigation on impingement dynamics and freezing performance of micrometer-sized water droplet on dry flat surface in supercooled environment. Int J Multiphase Flow 118:150–164
Sojka P, Guildenbecher D (2011) Experimental investigation of aerodynamic fragmentation of liquid drops modified by electrostatic surface charge. Atomization Sprays 21:139–147
Solomenko Z, Spelt PDM, Náraigh LÓ, Alix P (2017) Mass conservation and reduction of parasitic interfacial waves in level-set methods for the numerical simulation of two-phase flows: a comparative study. Int J Multiphase Flow 95:235–256
Stiti M, Castanet G, Labergue A, Lemoine F (2020) Icing of a droplet deposited onto a subcooled surface. Int J Heat Mass Transf 159:120116
Strotos G, Malgarinos I, Nikolopoulos N, Gavaises M (2016) Numerical investigation of aerodynamic droplet breakup in a high temperature gas environment. Fuel 181:450–462
Sun J, Gong J, Li G (2015) A lattice Boltzmann model for solidification of water droplet on cold flat plate. Int J Refrig 59:53–64
Sussman M, Smereka P, Osher S (1994) A level set approach for computing solutions to incompressible two-phase flow. J Comput Phys 114:146–159
Wang Y, Shu C, Huang HB, Teo CJ (2015a) Multiphase Lattice Boltzmann flux solver for incompressible multiphase flows with large density ratio. J Comput Phys 280:404–423
Wang Y, Shu C, Yang LM (2015b) An improved multiphase Lattice Boltzmann flux solver for three-dimensional flows with large density ratio and high Reynolds number. J Comput Phys 302:41–58
Wang L, Dai J, Hao P, He F, Zhang X (2020) Mesoscopic dynamical model of ice crystal nucleation leading to droplet freezing. Acs Omega 5:3322–3332
Wu Y, Gui N, Yang X, Tu J, Jiang S (2018) Improved stability strategies for pseudo-potential models of lattice Boltzmann simulation of multiphase flow. Int J Heat Mass Transf 125:66–81
Xu Z, Wang T, Che Z (2020) Droplet deformation and breakup in shear flow of air. Phys Fluids 32:052109
Yu Y, Li Q, Wen ZX (2020) Modified curved boundary scheme for two-phase lattice Boltzmann simulations. Comput Fluids 208:104638
Zhang Q, Qian T-Z, Wang X-P (2016) Phase field simulation of a droplet impacting a solid surface. Phys Fluids 28:022103
Zhang X, Liu X, Wu X, Min J (2018) Simulation and experiment on supercooled sessile water droplet freezing with special attention to supercooling and volume expansion effects. Int J Heat Mass Transf 127:975–985
Zhang X, Liu X, Min J, Wu X (2019) Shape variation and unique tip formation of a Sessile water droplet during freezing. Appl Therm Eng 147:927–934

Zhang C, Zhang H, Fang W, Zhao Y, Yang C (2020a) Axisymmetric lattice Boltzmann model for simulating the freezing process of a sessile water droplet with volume change. Phys Rev E 101:023314

Zhang X, Liu X, Wu X, Min J (2020b) Impacting-freezing dynamics of a supercooled water droplet on a cold surface: rebound and adhesion. Int J Heat Mass Transf 158:119997

Zhao H, Liu H-F, Li W-F, Xu J-L (2010) Morphological classification of low viscosity drop bag breakup in a continuous air jet stream. Phys Fluids 22:114103

Zhao H, Liu H-F, Xu J-L, Li W-F, Lin K-F (2013) Temporal properties of secondary drop breakup in the Bag-Stamen breakup regime. Phys Fluids 25:054102

Zhao J, Li X, Cheng P (2017) Lattice Boltzmann simulation of a droplet impact and freezing on cold surfaces. Int Commun Heat Mass Transf 87:175–182

Zhu C-L, Zhu C-X (2016) Aircraft icing and its protection. Science Press, Beijing